An IFN-STAT1-CYBB Axis Defines Protective Plasmacytoid DC to Neutrophil Crosstalk During *Aspergillus fumigatus* Infection.

Yahui Guo[1, 2, 3], Mariano A. Aufiero[1, 2, 3, 4], Kathleen A.M. Mills[1,2, 3, 5], Simon A. Grassmann[3], Hyunu Kim[3], Paul Zumbo[6], Mergim Gjonbalaj[1, 2, 3], Audrey Billips[1, 2, 3], Katrina B. Mar[1, 2, 3], Yao Yu[1, 2, 3], Doron Betel[7], Joseph C. Sun[3], Tobias M. Hohl[1, 2, 3, 4, 5, #]

[1]Infectious Disease Service, Department of Medicine, and [2]Human Oncology and Pathogenesis Program, and [3]Immunology Program, [4]Louis V. Gerstner Jr. Graduate School of Biomedical Sciences, Sloan Kettering Institute, Memorial Sloan Kettering Cancer Center, New York, NY10065, USA

[5]Immunology and Microbial Pathogenesis Graduate Program, Weill Cornell Graduate School, New York, NY 10065, USA

[6]Applied Bioinformatics Core, Department of Physiology and Biophysics, Weill Cornell Medicine, New York, NY 10065, USA.

[7]Applied Bioinformatics Core, Division of Hematology and Medical Oncology, Department of Medicine, Institute for Computational Biomedicine, Weill Cornell Medicine, New York, NY 10065, USA.

[#], Corresponding author and lead contact. E-mail: hohlt@mskcc.org (T.M.H.)

Footnote

[#]Address correspondence to:

Tobias M. Hohl, MD, PhD

Memorial Sloan Kettering Cancer Center

1275 York Avenue, Box 9

New York, NY 10065

Phone: 646-888-3596

Fax: 646-422-0502

hohlt@mskcc.org

Abstract

Aspergillus fumigatus is the most common cause of invasive aspergillosis (IA), a devastating infection in immunocompromised patients. Plasmacytoid dendritic cells (pDCs) regulate host defense against IA by enhancing neutrophil antifungal properties in the lung. Here, we define the pDC activation trajectory during *A. fumigatus* infection and the molecular events that underlie the protective pDC - neutrophil crosstalk. Fungus-induced pDC activation begins after bone marrow egress and results in pDC-dependent regulation of lung type I and type III IFN levels. These pDC-derived products act on type I and type III IFN receptor-expressing neutrophils and control neutrophil fungicidal activity and reactive oxygen species production via STAT1 signaling in a cell-intrinsic manner. Mechanistically, neutrophil STAT1 signaling regulates the transcription and expression of *Cybb*, which encodes one of five NADPH oxidase subunits. Thus, pDCs regulate neutrophil-dependent immunity against inhaled molds by controlling the local expression of a subunit required for NADPH oxidase assembly and activity in the lung.

Keywords: *Aspergillus fumigatus*, plasmacytoid DC, neutrophil, interferons, STAT1, NADPH oxidase, *Cybb*, lung, fungus, crosstalk

Introduction

Invasive pulmonary aspergillosis, a life-threatening mold infection, occurs when the respiratory immune system fails to eradicate ubiquitous inhaled *Aspergillus* spores (i.e., conidia) prior to their germination into tissue-invasive hyphae (Thompson and Young, 2021). At-risk populations include patients with acute leukemia and other bone marrow disorders, recipients of hematopoietic cell and lung transplants, individuals with immune-related or neoplastic diseases treated with prolonged corticosteroid therapy or with novel targeted biologics (e.g., ibrutinib) that blunt fungal immune surveillance pathways (Desai et al., 2024; Lionakis et al., 2017; Varughese et al., 2018) and patients with severe respiratory virus infections, including influenza and COVID-19 (Feys et al., 2024; Hoenigl et al., 2022). As a result of these medical advances and global pandemic viruses, *A. fumigatus* has become the most common agent of mold pneumonia worldwide (Brown et al., 2012; Feys et al., 2024; Latgé and Chamilos, 2019; Lionakis et al., 2023; Lionakis and Levitz, 2018; Mills et al., 2024; Tischler and Hohl, 2019).

Host defense against airborne mold conidia depends on intact myeloid cell numbers and function at the respiratory mucosa. Lung-infiltrating neutrophils and monocyte-derived dendritic cells (Mo-DCs) play essential roles in killing phagocytosed conidia, with a central role for products of NADPH oxidase in this process (Espinosa et al., 2017; Espinosa et al., 2014; Gerson et al., 1984; Varughese et al., 2018). Patients with chronic granulomatous disease (CGD) and defective NADPH oxidase function are uniquely vulnerable to invasive aspergillosis (IA, with a lifetime prevalence of 40-55% (Marciano et al., 2015). Exposure to products of NADPH oxidase induces a regulated cell death process in conidia trapped within neutrophil phagosomes, resulting in sterilizing immunity at respiratory mucosal barrier (Shlezinger et al., 2017).

An emerging theme of host defense against *Aspergillus* is the essential role of intercellular crosstalk to license neutrophil effector properties *in situ*. On one hand, recruited monocytes and Mo-DCs promote neutrophil ROS production through type I and III interferon (IFN) release, though the link between IFN production and neutrophil ROS activity remains undefined (Espinosa et al., 2017). On the other hand, we discovered that fungus-engaged neutrophils and Mo-DCs release CXCL9 and CXCL10 which results in the recruitment of $CXCR3^{+}$ pDCs by promoting their influx from the circulation into the lung. In the lung, pDCs enhance neutrophil fungicidal properties and are essential for host defense, even in the presence of lung-infiltrating monocytes and Mo-DCs (Guo et al., 2020). However, the underlying molecular mechanisms that regulate pDC to neutrophil crosstalk remain undefined. Thus, both Mo-DCs and pDCs independently enhance neutrophil antifungal activity, but it is unknown whether pDCs employ either similar or distinct mechanisms of intercellular crosstalk with neutrophils compared to monocytes and Mo-DCs. Critical open questions relate to the identity of pDC-derived molecules that are required for protective crosstalk with neutrophils and to the ensuing molecular changes in neutrophils that regulate antifungal activity *in situ*.

In this study, we demonstrate that pDCs represent a key and indispensable source of type I and type III interferons (IFNs) in the lung during respiratory *A. fumigatus* infection. In turn, pDC-dependent and IFN-induced STAT1 signaling controls neutrophil *Cybb* expression, which encodes an essential subunit of the NADPH oxidase complex. Thus, protective pDC to neutrophil crosstalk primarily harnesses intercellular IFN-STAT1 signaling to calibrate the synthesis of a critical component of the NADPH oxidase complex, thereby licensing neutrophils to achieve optimal antifungal activity and promoting sterilizing responses against inhaled mold spores.

Results

Aspergillus fumigatus induces pDC activation in the lung.

In response to respiratory fungal infection, pDCs exit the bone marrow (BM), enter the circulation, and traffic to the lung. To gain an understanding of the pDC activation trajectory during this infection-induced trafficking event, we conducted an unbiased transcriptome analysis of BM pDCs isolated from uninfected mice and of BM and lung pDCs isolated from mice at 72 h post-infection (pi), since this time point represents the peak of lung pDC influx (Fig. 1A, 1B, Supplemental Fig. S1A). For each pDC RNA-seq sample, we pooled sorted pDCs from 10 mice from each tissue examined and analyzed 4 biological replicates. The bulk pDC transcriptome was remarkably similar between naïve and infected BM pDCs, with only 51 differentially expressed genes, supporting a model in which pDC activation occurs en route to the site of infection. In these two groups of BM pDCs, we did not observe notable differences in the transcription of genes that encode cytokines or interferons (Fig. 1C, Supplemental Fig. S1B). In contrast, RNA-seq analysis revealed significant changes in the pDC transcriptome when lung pDCs were isolated from *Aspergillus*-infected mice and compared to BM pDCs from the same animals (Fig. 1B). Overall, pDCs from infected lungs had 4475 and 4474 differentially regulated genes compared to pDCs isolated from the BM of naïve and infected mice, respectively. (Fig.1C, Supplemental Fig. S1C and S1D). Using Kyoto Encyclopedia of Genes and Genomes (KEGG) pathway enrichment analysis, we found that pathways involved in the cytokine-cytokine receptor interaction, Toll-like receptor, RIG-I, and JAK-STAT signaling were among the most upregulated pathways in pDCs isolated from infected lungs compared to BM pDCs isolated from the same mice (Fig. 1D and Supplemental Fig. S1E).

Lung-infiltrating pDCs upregulated genes implicated in fungal recognition, including the C-type lectin receptors *Clec7a*, *Clec4n*, *Clec4d*, *Clec4e*, *Clec9a*, *Cd69* and *Cd209e* and downstream signaling molecules (*Card9* and *Syk*). pDCs upregulated Toll-like (*Tlr2*, *Tlr7*, *Tlr9*, and *Myd88)*, and growth factor (*Csf2ra*, *Csf2rb*) signaling pathways as well. Notably, we found that expression of type I interferon (IFN), type III IFN, and the type I IFN receptor (*Ifnar1* and *Ifnar2*), were markedly increased in lung-infiltrating pDCs isolated from infected mice (Fig. 1E), consistent with prior reports that *A. fumigatus* infection induces type I and type III IFN release in the lung (Espinosa et al., 2017). In addition, lung-infiltrating pDCs upregulated cytokine and chemokine (*Cxcl9*, *Cxcl10* and *Il12b)*, integrin receptor (i.e., *Icam1*, Intercellular Adhesion Molecule) and *Hif1a* mRNAs (Fig. 1E).

To examine the impact of pDC transcriptional changes on protein expression, we infected IFN-β reporter mice with *A. fumigatus* and found that *ifnb* promoter-driven fluorescent protein expression increased when BM pDCs trafficked to the lung (Fig. 1F and 1H). Similarly, we observed pDC trafficking-dependent increases in ICAM-1 surface expression (Fig. 1G and 1I). Thus, *A. fumigatus* infection substantially alters the pDC transcriptome at the portal of infection.

pDCs regulate type I and type III IFN in the lung during *A. fumigatus* infection.

To examine the contribution of pDCs to the lung inflammatory milieu, we examined type I (*Ifna1/2/5/6*) and type III (*Ifnl2/3*) IFN induction and found that induction peaked at 48 to 72 hpi (Fig. 1E and Fig. 2A-2C), temporally coincident with the peak lung pDC influx observed in a prior study (Guo et al., 2020). To determine whether pDCs directly control type I and type III induction, we infected BDCA2-DTR (pDC Depleter) mice, in which diphtheria toxin (DT) administration specifically ablates pDCs at rest and under inflammatory conditions (Swiecki et

al., 2010), but does not ablate -CC- chemokine receptor 2 (CCR2)-expressing monocytes and Mo-DCs that have been implicated in type I and type III IFN release following *A. fumigatus* infection (Espinosa et al., 2017; Guo et al., 2020). pDC depleter mice exhibited a 60-80% reduction in lung *Ifna1/2/5/6* and *Ifnl2/3* mRNA levels at 72 hpi, demonstrating that pDCs directly control the induction of type I and III IFN mRNA, consistent with the bulk RNA-seq data and with their activation trajectory in the *Aspergillus*-infected lung (Fig. 1E).

To measure the importance of pDCs for lung cytokine levels, we next compared lung cytokine profiles by ELISA from pDC-depleted mice and from non-transgenic, co-housed littermate controls. pDC ablation resulted in a partial depletion (40-60%) of lung type I (IFN-α2/4) and type III IFN levels (IFN-λ 2/3). In contrast, other pro-inflammatory cytokines implicated in pulmonary antifungal defense (GM-CSF, TNF, IL-1β, IL-6, and IL-12) were not impacted by pDC ablation, due to their production by other cellular sources (Mills et al., 2024) in the lung (Fig. 2E and 2F). These data establish that pDCs play a critical role in regulating lung type I and type III IFN levels during *A. fumigatus* infection.

STAT1 signaling in neutrophils controls the intracellular killing of *Aspergillus* conidia.

Type I and type III IFNs both activate STAT1 signaling in target cells and are essential for host defense against *A. fumigatus* (Espinosa et al., 2017). Under baseline conditions and during *Aspergillus* infection, lung neutrophils expressed both type I IFN receptor and type III IFN receptor mRNA, as judged by RNAscope analysis (Supplemental Fig. S2A and S2B), and both signal through STAT1. Targeted ablation of *Stat1* in neutrophils renders mice susceptible to invasive aspergillosis, yet it is unknown how STAT1 signaling is coupled to myeloid cell

antifungal activity and whether STAT1 signaling is required for killing in a myeloid cell-intrinsic or -extrinsic manner.

To distinguish these possibilities, we generated mixed BM chimeric mice (1:1 mixture of CD45.2^{+} *Stat1*$^{-/-}$ and CD45.1^{+} *Stat1*$^{+/+}$ donor BM cells → lethally irradiated CD45.1^{+} CD45.2^{+} *Stat1*$^{+/+}$ recipients) and compared the fungicidal activity of *Stat1*$^{-/-}$ and *Stat1*$^{+/+}$ leukocytes within the same lung inflammatory context (Fig. 3A). To accomplish this, we utilized fluorescent *Aspergillus* reporter (FLARE) conidia that encode a red fluorescent protein (DsRed; viability fluorophore) and are labeled with an Alexa Fluor 633 (AF633; tracer fluorophore) (Jhingran et al., 2016). FLARE conidia enable us to distinguish live (DsRed^{+}AF633^{+}) and dead (DsRed^{-} AF633^{+}) conidia during leukocyte interactions with single encounter resolution (Fig. 3B).

Following infection with FLARE conidia, we measured the frequency of neutrophil fungal uptake (Fig. 3C, frequency of neutrophil uptake = R1 + R2) and the proportion of fungus-engaged neutrophils that contain live conidia (Fig. 3C, proportion of fungus-engaged neutrophils with live conidia = R1/ (R1 + R2)). *Stat1*$^{-/-}$ neutrophils engulfed conidia at a slightly lower rate compared to *Stat1*$^{+/+}$ neutrophils in the same lung (Fig. 3D). However, the frequency of fungus-engaged neutrophils that contained live conidia was higher in *Stat1*$^{-/-}$ neutrophils compared to *Stat1*$^{+/+}$ neutrophils (Fig. 3E). Thus, neutrophil-engulfed conidia were more likely to be viable in *Stat1*$^{-/-}$ neutrophils than in *Stat1*$^{+/+}$ neutrophils in the same lung tissue environment (Fig. 3E), indicating that STAT1 signaling enhances neutrophil fungicidal activity in a cell-intrinsic manner. Consistent with these findings and in line with published studies (Espinosa et al., 2017) we found that mice that lacked *Stat1* in radiosensitive hematopoietic cells were more susceptible to *A. fumigatus* challenge than mice with *Stat1* sufficiency in the same compartment (Fig. 3F and

198 3G). *Stat1* expression in radiosensitive hematopoietic cells was dispensable for lung IFN-α2/4,
199 IFN-λ2/3, IL-1β, IL-6, IL-12p70, IL-23, and TNF levels (Supplemental Fig. S3A and 3H).
200 Our previous work found that lung pDCs regulate neutrophil ROS generation during
201 respiratory *A. fumigatus* challenge (Guo et al., 2020). Here we measured neutrophil ROS
202 production in *Stat1*$^{+/+}$ and *Stat1*$^{-/-}$ neutrophils and found that the ROS median fluorescence
203 intensity (MFI) in *Stat1*$^{-/-}$ ROS^{+} lung neutrophils were significantly reduced compared *Stat1*$^{+/+}$
204 ROS^{+} lung neutrophils at 72 hpi (Fig. 3I and 3J). We enumerated myeloid cells infiltration in
205 *Stat1*$^{+/+}$ and *Stat1*$^{-/-}$ lungs at 72 hpi, and found no difference in the recruitment of neutrophils,
206 monocyte, and pDCs in *Stat1*$^{-/-}$ mice. There was a slight decrease in Mo-DC numbers in *Stat1*$^{-/-}$
207 mice, which suggests that monocytes may exhibit a limited differentiation into Mo-DCs,
208 resulting in reduced lung Mo-DC numbers in *Stat1*$^{-/-}$ mice compared to control mice (Fig. S3B-
209 S3E).
210
211 **pDCs regulate neutrophil STAT1-dependent antifungal activity.**
212 To explore whether pDCs regulate neutrophil STAT1-dependent antifungal activity, we
213 bred CD45.2^{+} BDCA2-DTR$^{Tg/+}$ mice with CD45.2^{+} *Stat1*$^{-/-}$ mice to generate CD45.2^{+} BDCA2-
214 DTR$^{Tg/+}$ *Stat1*$^{-/-}$ mice and bred BDCA2-DTR$^{Tg/+}$ *Stat1*$^{+/+}$ mice to the CD45.1^{+} (C57BL6.SJL)
215 background. BM cells from both strains were mixed in a 1:1 ratio and utilized as donor cells to
216 generate mixed BM chimeric mice (CD45.1^{+} BDCA2-DTR$^{Tg/+}$ *Stat1*$^{+/+}$ and CD45.2^{+} BDCA2-
217 DTR$^{Tg/+}$ *Stat1*$^{-/-}$→ CD45.1^{+}CD45.2^{+} recipient mice). This experimental design enabled us to
218 compare the fungicidal activity of *Stat1*$^{+/+}$ and *Stat1*$^{-/-}$ neutrophils in the same lung, either in the
219 absence or in the presence of pDCs through the administration or omission of DT to mixed BM
220 chimeric mice (Fig. 4A).

This experimental approach yielded 4 groups of neutrophils that were analyzed 72 hpi with FLARE conidia. Group 1 (G1) neutrophils were *Stat1*$^{+/+}$ neutrophils isolated from pDC-sufficient mice; G2 neutrophils were *Stat1*$^{+/+}$ neutrophils isolated from pDC-ablated mice; G3 neutrophils were *Stat1*$^{-/-}$ neutrophils isolated from pDC-sufficient mice; and G4 neutrophils were *Stat1*$^{-/-}$ neutrophils isolated from pDC-ablated mice (Fig. 4A). There was no difference in conidial uptake among these four groups of neutrophils (Fig. 4B and 4C), indicating that pDCs do not control neutrophil conidial uptake and that neutrophil-intrinsic STAT1 signaling is dispensable for this process.

The frequency of neutrophils that contained live conidia was markedly increased in G3 (pDC^{+} lungs; *Stat1*$^{-/-}$) neutrophils compared to G1 (pDC^{+} lungs; *Stat1*$^{+/+}$) neutrophils (Fig. 4B and 4D), consistent with prior experimental results (Fig. 3E). Critically, pDC ablation increased the frequency of *Stat1*$^{+/+}$ neutrophils that contained live conidia (comparison of G2 versus G1 neutrophils; $P = 0.027$, Fig. 4B and 4D). This result indicates that pDC-derived products contribute to STAT1-dependent neutrophil conidiacidal activity. In contrast, pDC ablation did not significantly increase the frequency of *Stat1*$^{-/-}$ neutrophils that contained live conidia (comparison of G4 versus G3 neutrophils; $P = 0.09$, Fig. 4B and 4D).

To obtain a complementary measurement of pDC to neutrophil STAT1 crosstalk, we measured ROS production in the 4 neutrophil groups in parallel. Consistent with the direct measurements of fungicidal activity in Fig. 4D and with the ROS measurements in Fig. 3I and 3J, *Stat1*$^{+/+}$ neutrophils displayed a higher ROS mean fluorescence intensity (MFI) than *Stat1*$^{-/-}$ neutrophils (G1 versus G3). pDC ablation markedly reduced ROS production by *Stat1*$^{+/+}$ neutrophils (G2 versus G1), in line with the reduction in neutrophil fungicidal activity (Fig. 4E). In fact, *Stat1*$^{+/+}$ neutrophils isolated from pDC-depleted lungs (G2) had a similar ROS MFI as

244 *Stat1*$^{-/-}$ neutrophils isolated from pDC-sufficient lungs (G3). ROS levels observed in *Stat1*$^{-/-}$
245 neutrophils isolated from pDC-depleted lungs (G3) was lower than the ROS levels observed in
246 *Stat1*$^{-/-}$ neutrophils isolated from pDC-sufficient lungs (Fig. 4E), consistent with the idea that
247 pDCs can further modulate neutrophil ROS production in a *Stat1*-independent fashion.
248 Collectively, these findings indicate that pDCs regulate STAT1-dependent neutrophil fungicidal
249 activity and ROS production.
250
251 **STAT1-dependent guanylate-binding proteins are dispensable for the neutrophil anti-**
252 **fungal activity.**
253 To gain further insight into how STAT1 regulates cell-intrinsic neutrophil fungicidal
254 activity and ROS generation during respiratory *A. fumigatus* challenge, we generated mixed bone
255 marrow chimeric mice (1:1 mix of CD45.2^{+} *Stat1*$^{-/-}$ and CD45.1^{+} *Stat1*$^{+/+}$ donor bone marrow
256 cells → lethally irradiated CD45.1^{+}CD45.2^{+} *Stat1*$^{+/+}$ recipient mice) and performed bulk RNA-
257 seq on *Stat1*$^{-/-}$ and *Stat1*$^{+/+}$ neutrophils sorted from *A. fumigatus*-infected recipient mice. There
258 were marked differences in the transcriptome of *Stat1*$^{-/-}$ and *Stat1*$^{+/+}$ lung neutrophils (Fig. 5A),
259 with 2586 genes showing differential expression in *Stat1*$^{-/-}$ neutrophils compared to *Stat1*$^{+/+}$
260 neutrophils. KEGG pathway enrichment analysis showed downregulation of many pathways in
261 *Stat1*$^{-/-}$ neutrophils, including the cytosolic DNA sensing pathway, proteasome, RIG-I like
262 receptor signaling pathway, Toll-like receptor signaling pathway, cytokine-cytokine receptor
263 pathway (Fig. 5B). We identified commonly downregulated genes in *Stat1*$^{-/-}$ neutrophils, many
264 of which were known interferon-regulated genes (ISGs; Fig. 5C).
265 Several GTPases guanylate-binding proteins (GBPs), including *Gbp2*, *Gbp3*, *Gbp5* and
266 *Gbp7* were significantly downregulated in *Stat1*$^{-/-}$ neutrophils (Fig. 5C). To address the function

of these genes in neutrophil antifungal activity in otherwise immune competent mice, we utilized $Gbp^{chr3-/-}$ mice, which lack the entire chromosome 3 cluster that contains *Gbp1*, *Gbp2*, *Gbp3*, and *Gbp5*. We generated single chimeric mice ($CD45.2^{+}$ $Gbp^{chr3-/-}$ or $CD45.2^{+}$ $Gbp^{chr3+/+}$ → lethally irradiated $CD45.1^{+}$ $Gbp^{chr3+/+}$ recipients) (Fig. 5D) and compared the mortality and fungal burden of $Gbp^{chr3-/-}$ and $Gbp^{chr3+/+}$ chimeric mice. As expected from a prior study in corticosteroid and cyclophosphamide-treated mice (Briard et al., 2019), there was no difference in mortality or fungal colony forming unit (CFU) between $Gbp^{chr3-/-}$ and $Gbp^{chr3+/+}$ chimeric mice (Fig. 5E and 5F). Using mixed chimeric mice ($CD45.2^{+}$ $Gbp^{chr3-/-}$ and $CD45.1^{+}$ $Gbp^{chr3+/+}$ → $CD45.1^{+}CD45.2^{+}$ $Gbp^{chr3+/+}$ recipients) (Fig. 5G) and FLARE conidia, we quantified the cell-intrinsic antifungal activity of $Gbp^{chr3-/-}$ and $Gbp^{chr3+/+}$ leukocytes and found no difference in neutrophil conidial uptake and killing (Fig. 5H and 5I). Moreover, $Gbp^{chr3-/-}$ and $Gbp^{chr3+/+}$ neutrophils isolated from the same lung exhibited no difference in ROS MFI (Fig. 5J).

The pDC-IFN-STAT1 axis regulates neutrophil *Cybb* expression during A. *fumigatus* infection.

Since GBPs did not contribute to STAT1-regulated neutrophil defense against *A. fumigatus*, we investigated other candidate genes that were downregulated in $Stat1^{-/-}$ neutrophils (Fig. 5C) and focused next on *Cybb*, which encodes CYBB, the p91 subunit of the NADPH oxidase complex (NOX2). The four genes (*Cyba*, *Ncf1*, *Ncf2*, and *Ncf4*) that encode other subunits of the neutrophil NADPH oxidase complex (CYBA/p22 subunit, NCF1/p47 subunit, NCF2/p67 subunit and NCF4/p40 subunit) were not downregulated in $Stat1^{-/-}$ neutrophils (Fig. 6A). During *A. fumigatus* infection lung *Cybb* expression peaked at 48 and 72 hpi (Fig. S4A), temporally coincident with the observed peaks in lung pDC influx and type I and type III IFN

expression (Fig. 2A-C). The production of reactive oxygen species (ROS) by neutrophils is a vital mechanism for effectively eradicating fungal infections. Consistent with a prior study, we confirmed that *Cybb*-deficient mice (*gp91*$^{phox-/-}$) were highly susceptible to *A. fumigatus* infection (Fig. S4B) (Pollock et al., 1995). To investigate the hypothesis that STAT1 signaling in neutrophils regulates *Cybb* expression, we isolated neutrophils from infected *Stat1*$^{-/-}$ and *Stat1*$^{+/+}$ mice and found that *Cybb* mRNA level were decreased in *Stat1*$^{-/-}$ neutrophils compare to *Stat1*$^{+/+}$ neutrophils (Fig. 6B), consistent with STAT1-dependent regulation of *Cybb* transcription.

To determine chromatin accessibility at the *Cybb* locus, we performed assay for transposase-accessible chromatin (ATAC) sequencing of sorted *Stat1*$^{-/-}$ and *Stat1*$^{+/+}$ lung neutrophils from *A. fumigatus*-infected mice. Within the *Cybb* locus, we found three regions (blue squares) that were less accessible in *Stat1*$^{-/-}$ neutrophils than in *Stat1*$^{+/+}$ neutrophils (Fig. 6C), consistent with a modest STAT1-dependent regulation of *Cybb* expression (Fig. 6A and 6B). As a positive control, within Gbp2 locus, we found one region (red square) that was less accessible in *Stat1*$^{-/-}$ neutrophils compared to *Stat1*$^{+/+}$ neutrophils (Fig. 6C), consistent with STAT1-dependent regulation of *Gbp* expression (Fig. 5C).

To probe STAT1 binding to the Cybb gene locus, we performed Cleavage Under Targets & Release Using Nuclease (CUT&RUN) experiments of sorted *Stat1*$^{-/-}$ and *Stat1*$^{+/+}$ lung neutrophils from *A. fumigatus*-infected mice. We did not observe direct STAT1 binding to *Cybb* locus and promoter region (Fig. 6D). In CUT&RUN experiments, STAT1 bound to the *Gbp2* locus and promoter region (Fig. 6D). Collectively, these results suggest that STAT1 regulates *Cybb* transcription via an indirect mechanism.

Because STAT1 did not appear to regulate *Cybb* transcription through direct effects on chromosomal accessibility or binding to the *Cybb* locus, we next explored whether lung

neutrophil CYBB protein levels were regulated by STAT1 signaling. *Stat1*$^{-/-}$ and *Stat1*$^{+/+}$ neutrophils were isolated from *A. fumigatus* infected mice lungs at 72 hpi and analyzed for CYBB expression by Western blotting. CYBB protein levels, but not other subunits (p22/CYBA and p40/NCF4) of NADPH oxidase protein levels were lower in *Stat1*$^{-/-}$ neutrophils compared to *Stat1*$^{+/+}$ neutrophils (Fig. 6E – 6H), linking neutrophil STAT1 activation to CYBB expression, and to the oxidative burst.

Discussion

Our data introduce a model of protective pDC to neutrophil crosstalk in which pDCs undergo a defined activation trajectory in transit to the *Aspergillus*-infected lung. pDC activation provides a critical source of type I and type III IFN at the portal of infection, and licenses neutrophil antifungal properties in the lung in a direct manner. The latter step occurs through neutrophil-intrinsic STAT1-dependent control of CYBB protein levels. Local pDC-dependent control of NADPH oxidase assembly regulates the strength of neutrophil oxidative burst, as judged by reactive oxygen species production, boosts neutrophil intracellular conidial killing, and confers sterilizing immunity against inhaled spores.

pDCs originate in the bone marrow (BM), travel through the bloodstream, and migrate to lymphoid and nonlymphoid tissues during both normal and inflammatory states (Fujimura et al., 2015; Guo et al., 2020; Sozzani et al., 2010; Swiecki et al., 2017). In a recent study we demonstrated that *Aspergillus*-infected Mo-DCs and neutrophils release CXCR3 ligands (i.e., CXCL9 and CXCL10) into the inflamed lung, coupling fungal recognition and fungus-induced inflammation to CXCR3 signaling-dependent pDC influx from the circulation into the lung. In this study, *A. fumigatus* infection induces a pDC activation trajectory that substantially alters the

lung rather than the BM pDC transcriptome, implying that pDC trafficking to peripheral tissue precedes activation occurs at the portal of infection. While not a focus of this work, the precise mechanism of pDC activation in the fungus-infected lung remains an open question, in part because conditional gene deletion strategies do not exist for pDCs, precluding facile comparison of gene-deficient and gene-sufficient pDCs in infected tissues in mice with no other genetic perturbations.

Our data indicate that lung-infiltrating pDCs upregulate genes implicated in fungal recognition, including the C-type lectin receptors (CLRs) and downstream signaling molecules. pDCs express the C-type lectin receptors Dectin-1, Dectin-2, and Dectin-3 and can secrete IFN-α and TNF when co-incubated with *Aspergillus* hyphae via Dectin-2 signaling (Maldonado et al., 2022; Seeds et al., 2009; Taylor et al., 2002), though the interaction of pDCs with conidia, the infectious propagules, were not examined. pDCs do not internalize *Aspergillus* conidia readily in the test tube or in the infected lung (Desai et al., 2024; Maldonado et al., 2022), supporting the notion that activation occurs via fungal cell contact or via the presence of activating cytokines or other inflammatory mediators. Support for the latter scenario comes from an experiment in which curdlan (i.e., a particulate Dectin-1 agonist)-induced upregulation of pDC CD40 and CD83 expression could be increased by simultaneous co-incubation with an acellular curdlan-stimulated peripheral blood mononuclear cell supernatant (Maldonado et al., 2022). Beyond *Aspergillus*, pDC-enriched human cell fractions can release TNF in a Dectin-2- and Dectin-3-signaling-dependent fashion in response to *Paracoccidioides brasiliensis* co-incubation (Preite et al., 2018). Beyond CLR signaling, we found that *Aspergillus* infection triggered upregulation of Toll-like receptors in lung-infiltrating pDCs. Prior work demonstrated that *Aspergillus*-derived unmethylated CpG sequences can activate TLR9 signaling *in vitro* (Herbst et al., 2015; Ramirez-

359 Ortiz et al., 2008), and this may represent an additional mechanism by which pDCs become
360 activated *during Aspergillus* infection.

361 During Dengue, Zika, and Hepatitis C viral infections, physical contact with virally
362 infected cells stimulates pDC-mediated antiviral responses (Assil et al., 2019; Webster et al.,
363 2018). $\alpha_L\beta_2$ integrin (lymphocyte function-associated antigen-1; LFA-1) expressed by the pDC
364 can bind to ICAM-1 on infected cells to promote a sustained interaction, termed an
365 interferonogenic synapse, during which viral RNA is transferred to pDCs, leading to IFN
366 production via the nucleic acid sensor TLR7. This process activates type I IFN-dependent
367 antiviral programs in infected tissues. pDC commitment to type I IFN production is further
368 regulated by antecedent cell-intrinsic TNF receptor and leukemia inhibitory factor signaling
369 during murine cytomegalovirus infection, underscoring the contribution of local cytokine
370 signaling to pDC activation by contact-dependent and -independent mechanisms (Abbas et al.,
371 2020). The lung pDC transcriptomic data detected increased expressed ICAM-1 in the lung-
372 infiltrating pDCs isolated from infected mice. This observation raises the possibility that ICAM-
373 1 expression may facilitate lung pDC contact with β_2-integrin-expressing myeloid cells to
374 facilitate reciprocal interactions. In sum, the upregulation of multiple receptors from various
375 classes suggests that pDCs likely employ a blend of receptors to identify and react to fungal
376 pathogens, leading to full pDC activation in the fungus-infected lung. Notably, we were unable
377 to isolate sufficient pDCs to compare the bulk lung pDC transcriptome in naïve mice with the
378 lung pDC transcriptome in *Aspergillus*-infected mice.

379 Recent studies have advanced the concept that circulating neutrophils exhibit
380 transcriptional heterogeneity in the steady state and during microbial infection (Xie et al., 2020).
381 In addition, neutrophils can acquire transcription-dependent non-canonical functions upon entry

into peripheral tissues, exemplified by a regulatory role in angiogenesis in the lung (Ballesteros et al., 2020). Single-cell analysis has revealed the presence of three separate circulating murine and human populations that differ with respect to interferon-stimulated gene (ISG) and CXCR4 expression. Interestingly, all three populations expressed similar levels of *Cybb* mRNA and exhibited similar NADPH oxidase scores by gene ontogeny analysis during homeostasis and systemic bacterial (i.e., *Escherichia coli*) infection (Xie et al., 2020). During tuberculosis, malaria, and hematopoietic cell transplantation, circulating human neutrophils exhibit an IFN transcriptional signature (Berry et al., 2010; Montaldo et al., 2022; Rocha et al., 2015), which in the case of malaria, is reduced by receipt of anti-malarial therapy. The finding that pDC-derived type I and type III IFN licenses neutrophil antifungal activity through STAT1-dependent control of *Cybb* transcription and CYBB protein levels raises the important question whether the ISG^{hi} neutrophil subset is enriched in the lung and particularly effective at killing *Aspergillus* conidia compared to the other two ISG^{lo} circulating subsets. The ability to track and quantify fungal uptake killing with FLARE conidia will facilitate future studies to link lung-infiltrating neutrophil subsets, defined by distinct transcriptional profiles, to the quality of effector functions at single-encounter resolution. These studies support idea that dynamic transcriptional plasticity represents a cardinal feature of the circulating neutrophil response to microbial infection and other external stressors. It remains unclear whether the observed transcriptional plasticity represents dynamic changes in the production of transcriptionally heterogeneous circulating neutrophil subsets or represents an interconversion between circulating subsets.

The effects of type III IFN on neutrophils are context-dependent. In a DSS model of sterile colitis, IFN- λ has been linked to neutrophil ROS suppression and a reduction in neutrophil degranulation (Broggi et al., 2017). In human neutrophils, recombinant IFN- λ can

inhibit platelet-induced NETosis (Chrysanthopoulou et al., 2017). IFN-λ has various roles in bacterial infections (Ardanuy et al., 2020; Lazear et al., 2015), with a previous study demonstrated that *Bordetella pertussis* infection induces IFN-λ and IFN-λ receptor (IFNLR1) expression as well as inflammation in the lung (Ardanuy et al., 2020). IFN-λ signaling in neutrophils can suppress *B. pertussis* killing and neutrophil production of ROS, MMP9, NETs, MPO, and IFN-γ (Antos et al., 2024; Kumar et al., 2024). In contrast, conditional deletion of the IFN-λ receptor in neutrophils is linked to a reduction in neutrophil ROS during pulmonary *A. fumigatus* infection (Espinosa et al., 2017). During HSV corneal infection, application of recombinant IFN-λ suppressed neutrophil recruitment but did not impact virucidal activity or ROS production (Antony et al., 2021). These results indicate that IFN-λ may have different biological effects based on cellular targets and responsiveness at sites of inflammation and on the type of inflammatory stimulus. In this study, the STAT1-dependent action of pDC-dependent IFNs (both type I and III) on neutrophils is critical for their local licensing of their cell-intrinsic cytotoxic activity against *Aspergillus* conidia. The individual contribution of type I versus type III IFN-dependent activation on STAT1-dependent CYBB expression remains unclear. An open question remains how STAT1 signaling precisely regulates *Cybb* transcription and CYBB translation, since we could not detect clear evidence of STAT1 binding to the *Cybb* promoter or clear STAT1-dependent changes in chromatin accessibility.

Overall, these findings provide important insights into the pDC-STAT1-CYBB axis as a key regulator of NADPH oxidase expression and highlight the critical role of this pathway in promoting antifungal immunity in neutrophils. The discovery that pDCs can regulate ROS induction by neutrophils by controlling the STAT1-dependent expression of a single NADPH

oxidase subunit adds to our understanding of the complex and protective interplay between innate immune cells during fungal infection.

ACKNOWLEDGMENTS

We thank Dr. Thirumala-Devi Kanneganti (St. Jude Children's Research Hospital) providing the *GBP*$^{chr3-/-}$ bone marrows. We thank the MSKCC IGO core for performing RNA sequencing, and Chen Liao (Geisel School of Medicine at Dartmouth), Paul Zumbo (Weill Cornell Medicine) for assistance with the RNA sequencing data analysis. We thank Robert Cramer (Geisel School of Medicine at Dartmouth), Iliyan Iliev (Weill Cornell Medicine), and members of the Hohl laboratory for numerous conversations and insights into this study. In this study, T. M. H. was supported by NIH grants P30 CA 008748 (to MSKCC), R37 AI093808, and R01 AI139632; Y. G. was supported by the Ludwig Center Post-Doctoral Award, MSKCC; M.A.A. was supported by NIH F31 AI161996; K.A.M.M. was supported by NIH F31 AI167511; K. B. M. was supported by Experimental Immuno-oncology Scholars' Program, MSKCC and NIH 5T32CA009149; J. C. S. was supported by the Ludwig Center for Cancer Immunotherapy, the American Cancer Society, the Burroughs Wellcome Fund, and the NIH grants R01 AI100874, R01 AI130043, R01 AI155558, and P30CA008748. S. G. was supported by CRI / Donald J. Gogel Postdoctoral Fellowship CRI Award CRI3934 and NIH K99AI180360. The funders had no role in study design, data collection and analysis, decision to publish or preparation of manuscript. We acknowledge the use of the Integrated Genomics Operation Core, funded by the NCI Cancer Center Support Grant (CCSG, P30 CA08748), Cycle for Survival, and the Marie-Josée and Henry R. Kravis Center for Molecular Oncology.

AUTHOR CONTRIBUTIONS

Conceptualization, T.M.H., and Y.G.; Methodology, T.M.H., and Y.G.; Investigation, Y.G., M.A.A., K.A.M.M, S. A. G., H. K., P. Z., M.G., A.B., K.M., Y. Y.; Writing – Original Draft, Y.G. and T.M.H.; Writing – Review & Editing, Y.G. and T.M.H.; Funding Acquisition, T.M.H. and Y.G.; Resources, J. S., and D. B.

DECLARATION OF INTERESTS

The authors declare no competing interests.

MATERIALS AND METHODS

Chemicals and reagents

Unless otherwise noted, chemicals were purchased from Sigma-Aldrich or Fisher Scientific, cell culture reagents from Thermo Fisher Scientific, and microbiological culture media from BD Biosciences. Antibodies for flow cytometry were acquired from BD Biosciences, Thermo Fisher Scientific and Tonbo.

Mice

C57BL/6J (JAX: 00664), BDCA2-DTR (JAX: 014176) mice were from Jackson Laboratories. *GBP*$^{chr3-/-}$ bone marrows were provided by Dr. Thirumala-Devi Kanneganti. C57BL/6.SJL (Stock: 4007) were purchased from Taconic. C57BL/6 and C57BL/6.SJL mice were crossed to generate CD45.1^{+}CD45.2^{+} recipient mice for mixed BM chimeras. CD45.2^{+} BDCA2-DTR$^{Tg/+}$ were backcrossed to C57BL/6.SJL mice to obtain CD45.1^{+} BDCA2- DTR$^{Tg/+}$

mice. BDCA2- DTR$^{Tg/+}$ were crossed with CD45. 2^{+} *Stat1*$^{-/-}$ mice to obtain CD45. 2^{+} BDCA2- DTR$^{Tg/+}$ *Stat1*$^{-/-}$ mice. For experiments in which the breeding strategy did not yield littermate controls, gene-knockout mice were co-housed with C57BL/6 mice for 14 days prior to infection, whenever possible. All mouse strains were bred and housed in the MSKCC or St. Jude Children's Research Hospital Animal Resource Center under specific pathogen-free conditions. All animal experiments were conducted with sex- and age-matched mice and performed with MSKCC Institutional Animal Care and Use Committee approval. Animal studies complied with all applicable provisions established by the Animal Welfare Act and the Public Health Services Policy on the Humane Care and Use of Laboratory Animals.

Generation of Bone Marrow Chimeric Mice

For single BM chimeras, CD45.1^{+} C57BL/6.SJL recipients were lethally irradiated (900cGy), reconstituted with either 2-5 × 10^{6} CD45.2^{+} *GBP*$^{chr3-/-}$, CD45.2^{+} C57BL/6J or CD45.2^{+} *Stat1*$^{-/-}$ BM cells. For mixed BM chimeras, CD45.1^{+}CD45.2^{+} recipients were irradiated and reconstituted with a 1:1 mixture of CD45.1^{+} C57BL/6.SJL and CD45.2^{+} *Stat1*$^{-/-}$ or CD45.2^{+} *GBP*$^{chr3-/-}$ BM cells, CD45.1^{+} BDCA2- DTR$^{Tg/+}$ and CD45.2^{+} BDCA2- DTR$^{Tg/+}$ *Stat1*$^{-/-}$. After BM transplantation, recipient mice received 400 μg/ml enrofloxacin in the drinking water for 21 days to prevent bacterial infections and rested for 6-8 weeks prior to experimental use.

***Aspergillus fumigatus* Infection Model**

A. fumigatus Af293, Af293-dsRed (Jhingran et al., 2016), and CEA10 (Girardin et al., 1993) strains were cultured on glucose minimal medium slants at 37^{o}C for 4-7 days prior to harvesting conidia for experimental use. To generate FLARE conidia, briefly, 7 × 10^{8} Af293-

dsRed conidia were rotated in 10 µg/ml Biotin XX, SSE in 1 ml of 50 mM carbonate buffer (pH 8.3) for 2 hr at 4 ºC, incubated with 20 µg/ml Alexa Fluor 633 succinimidyl ester at 37 ºC for 1 h, resuspended in PBS and 0.025% Tween 20 for use within 24 hrs. (Heung et al., 2015; Jhingran et al., 2016). To generate morphologically uniform heat-killed swollen conidia, 5×10^6/ml conidia were incubated at 37^o C for 14 hours in RPMI-1640 and 0.5 µg/ml voriconazole and heat killed at 100 ºC for 30 minutes (Hohl et al., 2005). To infect mice with 30-60 million live or heat-killed *A. fumigatus* cells, conidia were resuspended in PBS, 0.025% Tween-20 at a concentration of 0.6-1.2$\times10^9$ cells and 50 µl of cell suspension was administered via the intranasal route to mice anesthetized by isoflurane inhalation.

Analysis of *in vivo* and *in vitro* conidial uptake and killing

To analyze of conidia uptake and killing, FLARE conidia were used to infect mice. In data analyses for a given leukocyte subset, conidial uptake refers to the frequency of fungus-engaged leukocytes, i.e., the sum of dsRed$^+$ AF633$^+$ and dsRed$^-$ AF633$^+$ leukocytes. Conidial viability within a specific leukocyte subset refers to the frequency of leukocytes that contain live conidia (dsRed$^+$ AF633$^+$) divided by the frequency of all fungus-engaged leukocytes (dsRed$^+$ AF633$^+$ and dsRed$^-$ AF633$^+$).

***In vivo* Cell Depletion**

To ablate specific cells, BDCA2- DTR$^{Tg/+}$, BDCA2- DTR$^{Tg/+}$ *Stat1*$^{-/-}$, and non-transgenic littermate controls were injected i.p. with 10 ng/g body weight DT on Day -1, Day 0, and Day +2 pi (Swiecki et al., 2010), unless noted otherwise.

519

520 **Analysis of Infected Mice**

521 To prepare single cell lung suspensions for flow cytometry, we followed the method
522 outlined in (Hohl et al., 2009) with minor modifications. After perfusing murine lungs, they were
523 placed in a gentle MACS™ C tube and mechanically homogenized in 5 ml RPMI-1640, 10%
524 FBS, and 0.1 mg/ml DNAse using a gentle MACS™ Octo Dissociator (Miltenyi Biotech)
525 without the use of collagenase. The lung cell suspensions were then lysed of RBCs, enumerated,
526 and stained with fluorophore-conjugated antibodies prior to flow cytometric analysis. We used
527 either a Cytoflex or a BD Aria for flow cytometric sorting and performed flow plot analysis
528 using FlowJo v.9.6.6 software.

529 Neutrophils were identified as $CD45^+$ $CD11b^+$ $Ly6C^{lo}$ $Ly6G^+$ cells, monocytes as
530 $CD45^+$ $CD11b^+$ $CD11c^-$ $Ly6G^-$ $Ly6C^{hi}$ cells, Mo-DCs as $CD45^+$ $CD11b^+$ $CD11c^+$ $Ly6G^-$
531 $Ly6C^{hi}$ MHC class II^+ cells, and pDCs as $CD45^+$ $CD11c^{int}$ $SiglecF^-$ $CD19^-$ $NK1.1^-$ $CD11b^-$
532 $B220^+$ $SiglecH^+$ cells.

533 To assess the lung fungal burden, perfused murine lungs were homogenized using a
534 PowerGen 125 homogenizer (Fisher) in 2 mL of PBS containing 0.025% Tween-20 and plated
535 onto Sabouraud dextrose agar. For analysis of cytokine levels by ELISA, whole lungs were
536 weighed and mechanically homogenized in 2 mL of PBS containing protease inhibitors. To
537 analyze cytokine levels by qRT-PCR, we extracted total RNA from cells using TRIzol
538 (Invitrogen). One to two micrograms of total RNA were reverse-transcribed using the High-
539 Capacity cDNA Reverse Transcription Kit (Applied Biosystems). We used TaqMan Fast
540 Universal Master Mix (2×) and TaqMan probes (Applied Biosystems) for each gene and

normalized to glyceraldehyde-3-phosphate dehydrogenase. Gene expression was calculated using the Ct method relative to the naïve sample.

Intracellular ROS levels were measured in cells using CM-H2DCFDA [5-(and 6-) chloromethyl-2,7-dichlorodihydrofluorescein diacetate, acetyl ester] as described in (Hackstein et al., 2012). Briefly, single cell lung suspensions were incubated with 1µM CM-H2DCFDA in Hanks' balanced salt solution at 37º C for 45 min according to manufacturer's instruction and analyzed by flow cytometry.

Immunoblotting assay

Cells were lysed in lysis buffer (150 mM NaCl, 50 mM HEPES (pH 7.4), 1 mM EDTA, 1% Nonidet P-40, protease inhibitors). Total cell lysates were subjected to SDS-PAGE and then blotted using indicated antibodies, Cybb polyclonal antibody (Invitrogen, cat. no. PA5-76034), p22phox mAb (CST, cat. no. 37570), p40phox mAb (cat. no. AB76158), GAPDH mAb (CST, cat. no. 5174s).

RNA sequencing

RNA extraction. Phase separation in cells lysed in 1 mL TRIzol Reagent (ThermoFisher cat. no. 15596018) was induced with 200 µL chloroform. RNA was extracted from 350 µL of the aqueous phase using the miRNeasy Micro or Mini Kit (Qiagen cat. no. 217084/217004) on the QIAcube Connect (Qiagen) according to the manufacturer's protocol. Samples were eluted in 13-15 µL RNase-free water.

Transcriptome sequencing. After RiboGreen quantification and quality control by Agilent BioAnalyzer, 1.9-2.0 ng total RNA with RNA integrity numbers ranging from 7.8 to 10 underwent amplification using the SMART-Seq v4 Ultra Low Input RNA Kit (Clonetech cat. no. 63488), with 12 cycles of amplification. Subsequently, 7.4-10 ng of amplified cDNA was used to prepare libraries with the KAPA Hyper Prep Kit (Kapa Biosystems cat. no. KK8504) using 8 cycles of PCR. Samples were barcoded and run on a HiSeq 4000 or NovaSeq 6000 in a PE50 (HiSeq) or PE100 (NovaSeq) run, using the HiSeq 3000/4000 SBS Kit or NovaSeq 6000 S4 Reagent Kit (200 Cycles) (Illumina). An average of 40 million paired reads were generated per sample and the percent of mRNA bases per sample averaged 84%.

RNA-Sequencing data analysis. Raw reads were quality checked with FastQC v0.11.7 (http://www.bioinformatics.babraham.ac.uk/projects/fastqc/), and adapters were trimmed using Trim Galore v0.6.7 (http://www.bioinformatics.babraham.ac.uk/projects/trim_galore/). Reads were aligned to the mouse reference genome (GRCm38.p6) using STAR v2.6.0c (Dobin et al., 2013) with default parameters. Gene abundances were calculated with featureCounts v1.6.2 (Liao et al., 2014) using composite gene models from Gencode release vM17 . Principle component analysis was performed using the plotPCA function from DESeq2 v1.32.0 (Love et al., 2014). Differentially expressed genes were determined with DESeq2 v1.32.0 with a two-factor model incorporating batch as a covariate, with significance determined by Wald tests ($q < 0.05$). Gene set enrichment analysis was performed using fgsea v1.18.0 (Korotkevich et al., 2019) with gene sets from the Broad Institute's MSigDB (Loures et al., 2015; Subramanian et al., 2005) collections; genes were ranked by the DESeq2 Wald statistic. Only pathways with an adjusted P value < 0.05 were considered enriched. Expression heatmaps were generated using variance-

stabilized data, with the values centered and scaled by row. Code has been deposited to GitHub (https://github.com/abcwcm/Guo2024).

RNAscope microscopy

Formaldehyde-fixed, paraffin embedded (FFPE) surgical tissue Sects. FFPE tissue sections (5 µm) were processed exactly as described in the manufacturer's instructions (ACD Bio, cat. no. 323100). Probes targeting the following genes were used: Ly6G (ACD Bio, cat. no. 455701-C3), IFNλR (ACD Bio, cat. no. 512981-C1), IFNαR1(ACD Bio, cat. no. 512971-C2). Slides were mounted with Prolong Diamond mounting media (ThermoFisher Scientific, cat. no. P36965). Slides were scanned using a Pannoramic Digital Slide 517 Scanner (3DHISTECH, Budapest, Hungary) using a 20×/0.8NA objective.

Assay for transposase-accessible chromatin (ATAC) sequencing and epigenome analyses

Freshly harvested WT and KO mouse neutrophils were directly sent to MSKCC's Epigenetics Research Innovation Lab. ATAC was performed as previously described (Corces et al. Nature Methods 2017) using 50,000 cells per replicate and the Tagment DNA TDE1 Enzyme (Illumina, 20034198). Sequencing libraries were prepared using the ThruPLEX DNA-Seq Kit (Takarabio, R400676) and sent to the MSKCC Integrated Genomics Operation core facility for sequencing on a NovaSeq 6000. Raw sequencing reads were trimmed and filtered for quality (Q>15) and adapter content using version 0.4.5 of TrimGalore (https://www.bioinformatics.babraham.ac.uk/projects/trim_galore) and running version 1.15 of cutadapt and version 0.11.5 of FastQC. Version 2.3.4.1 of bowtie2 (http://bowtie-bio.sourceforge.net/bowtie2/index.shtml) was employed to align reads to mouse assembly mm10

and alignments were deduplicated using Mark Duplicates in Picard Tools v2.16.0. Enriched regions were discovered using MACS2 (https://github.com/taoliu/MACS) with a p-value setting of 0.001, filtered for blacklisted regions (http://mitra.stanford.edu/kundaje/akundaje/release/blacklists/ mm10-mouse/mm10.blacklist.bed.gz), and a peak atlas was created using +/- 250 bp around peak summits. The BEDTools suite (http://bedtools.readthedocs.io) was used to create normalized bigwig files. Version 1.6.1 of featureCounts (http://subread.sourceforge.net) was used to build a raw counts matrix and DESeq2 was employed to calculate differential enrichment for all pairwise contrasts. Peak-gene associations were created by assigning all intragenic peaks to that gene, while intergenic peaks were assigned using linear genomic distance to transcription start sites (TSS).

Histone and Transcription Factor CUT&RUN

For CUT&RUN, 400,000 sorted neutrophils were used for H3K4me3 and STAT1 analysis. Anti-H3K4me3 (Epicypher, cat. no. 13-0028) or polyclonal anti-STAT1 antibodies (Proteintech, cat. no. 10144-2-AP) were employed for each target. Sorted cells were washed with PBS and resuspended in Antibody Buffer (1 × eBioscience Perm/Wash Buffer, 1× Roche cOmplete EDTA-free Protease Inhibitor, 0.5 µM Spermidine, and 2 µM EDTA in H2O). They were incubated overnight at 4°C with control IgG, H3K4me3, or STAT1 antibodies diluted 1:100 in Antibody Buffer in a 96-well V-bottom plate. Following antibody incubation, cells were washed twice with Buffer 1 (1× eBioscience Perm/Wash Buffer, 1× Roche cOmplete EDTA-free Protease Inhibitor, 0.5 µM Spermidine in H2O) and resuspended in 50 µL of Buffer 1 plus 1× pA/G-MNase (Cell Signaling, cat. no. 57813). This mixture was incubated on ice for 1 hour, then

washed twice with Buffer 2 (0.05% w/v Saponin, 1× Roche cOmplete EDTA-free Protease Inhibitor, 0.5 µM Spermidine in 1X PBS) three times. Cells were resuspended in Calcium Buffer (Buffer 2 plus 2 µM CaCl2) and incubated on ice for 30 minutes to activate the pA/G-MNase reaction. An equal volume of 2× STOP Buffer (Buffer 2 plus 20 µM EDTA plus 4 µM EGTA) and 1 pg of *Saccharomyces cerevisiae* spike-in DNA (Cell Signaling, cat. no. 29987) were added. Samples were incubated at 37 °C for 15 minutes, followed by DNA isolation and purification using the Qiagen MinElute Kit per the manufacturer's instructions.

Immunoprecipitated DNA was quantified by PicoGreen, and the size was evaluated using an Agilent BioAnalyzer: fragments between 100 and 600 bp were size selected using aMPure XP beads (Beckman Coulter, cat. no. A63882). KAPA HTP Library Preparation Kit (Kapa Biosystems, cat. no. KK8234) was used to prepare Illumina sequencing libraries according to the manufacturer's instructions with 0.001–0.5 ng input DNA and 14 cycles of PCR. Barcoded libraries were run on the NovaSeq 6000 in a PE100 run using S4 kit version 1.5 with XP mode to generate approximately 23 million paired reads per sample.

CUT&RUN Data Processing

CUT&RUN datasets were processed by trimming paired reads for adaptors and low-quality sequences using Trimmomatic (v0.39) and aligning to the mm10 reference genome with Bowtie 2 (v2.4.1). Peaks were identified using MACS2 (v2.2.7.1) with input samples as control, employing narrow peak parameters and cutoff - analysis - ple-5 - keep - dup all -B - SPMR. Irreproducible discovery rate (IDR) calculations were performed using ENCODE project scripts (IDR v2.0.4.2). Reproducible peaks with an IDR value of 0.05 or less in each condition were retained, aggregated, and merged to create the final atlas, which was annotated with the UCSC

Known Gene model. Reads were mapped to this atlas and counted using the summarize Overlaps function from the Genomic Alignment package (v1.34.1).

Visualization. Genomic tracks were visualized using GViz (v1.42.1) or IGV (v2.9.4).

Quantitation and Statistical Analysis

All data presented are representative of at least two independent experiments, as indicated. Unless stated otherwise, all results are expressed as mean (± SEM). We used the Mann-Whitney test for comparisons of two groups, and the Kruskal-Wallis test for multi-group comparisons, unless noted otherwise. Survival data were analyzed using the long-rank test. All statistical analyses were performed using GraphPad Prism software (v9.2.0).

RESOURCE AVAILABILITY Lead Contact

Further information and requests for resources or reagents should be directed to the Lead Contact, Tobias M. Hohl (hohlt@mskcc.org).

Materials Availability

This study did not generate new unique reagents.

Data and Code Availability

RNA sequencing data, ATAC sequencing data and CUT&RUN sequencing data were uploaded into NCBI database. Raw RNA sequencing datasets generated in this study are available at GSE280164. Raw ATAC sequencing data and CUT&RUN sequencing data generated in this study are available at GSE280229.

677

678 **Key Resources Table**

REAGENT or RESOURCE	SOURCE	IDENTIFIER
Antibodies		
APC Mouse anti-Mouse CD45.1 (clone A20)	BD Bioscience	Cat#558701; RRID: AB_1645214
PerCP-Cy™5.5 Mouse anti-Mouse CD45.2 (clone 104)	BD Bioscience	Cat#552950; RRID: AB_394528
APC-Cy™7 Rat anti-Mouse CD45 (clone 30-F11)	BD Bioscience	Cat#557659; RRID: AB_396774
PerCP-Cy™5.5 Rat anti-CD11b (clone M1/70)	BD Bioscience	Cat#550993; RRID: AB_394002
PE-Cy™7 Hamster anti-Mouse CD11c (clone HL3)	BD Bioscience	Cat#558079; RRID: AB_647251
BV 605™ anti-mouse CD11c Antibody (clone N418)	BioLegend	Cat#117334; RRID: AB_117334
PE-Cy™7 Rat Anti-Mouse Ly-6C (clone AL-21)	BD Bioscience	Cat#560593; RRID: AB_1727557
FITC Rat anti-Mouse Ly-6G (clone 1A8)	BD Bioscience	Cat#551460; RRID: AB_394207
FITC Rat anti-Mouse CD45R/B220 (clone RA3-6B2)	BD Bioscience	Cat#553087; RRID: AB_394617
PE anti-mouse CD183 Antibody (clone CXCR3-173)	BioLegend	Cat#126505; RRID: AB_1027656
BV421 Rat Anti-Mouse Siglec-F (clone E50-2440)	BD Bioscience	Cat#562681; RRID: AB_2722581

BV605 Rat Anti-Mouse Siglec-H (clone 440c)	BD Bioscience	Cat#747673; RRID: AB_2744234
Purified Rat Anti-Mouse CD16/CD32 (clone 2.4G2)	BD Bioscience	Cat#553142; RRID: AB_394657
eFluor 450 NK1.1 Monoclonal Antibody (clone PK136)	eBioscience	Cat#48-5941-80; RRID: AB_2043878
eFluor 450 CD19 Monoclonal Antibody (clone eBio1D3)	eBioscience	Cat#48-0193-82; RRID: AB_2734905
Alexa Fluor 700, I-A/I-E Monoclonal Antibody (clone M5/114.15.2)	eBioscience	Cat#56-53-21; RRID: AB_494009
FITC Mouse IgG1 kappa Isotype Control	eBioscience	Cat#11-4714-42; RRID: AB_10596964
PE Rat IgG2a kappa Isotype Control	eBioscience	Cat#12-4321-42; RRID: AB_1518773
PerCP-Cyanine5.5 IgG Isotype Control	eBioscience	Cat#45-4888-80; RRID: AB_906260
APC Rat IgG2b kappa Isotype Control	eBioscience	Cat#17-4031-82; RRID: AB_470176
APC-eFluor 780 Rat IgG2b kappa Isotype Control	eBioscience	Cat#47-4031-80; RRID: AB_1272021
Alexa Fluor 700 Rat IgG2b kappa Isotype Control	eBioscience	Cat#56-4031-80; RRID: AB_837123
PE-Cyanine7 Rat IgG2a kappa Isotype Control	eBioscience	Cat#25-4321-82; RRID: AB_470200
eFluor 450 Rat IgG1 kappa Isotype Control	eBioscience	Cat#48-4301-82; RRID: AB_1271984

Bacterial and Virus Strains		
AF293	Fungal genetics stock center	#A1100
AF293 ds-Red	(Jhingran et al., 2016)	N/A
CEA10 (also known as CBS144.89)	(Girardin et al., 1993)	Received form Robert A. Cramer
Chemicals, Peptides, and Recombinant Proteins		
Alexa Fluor 633 succinimidyl ester	Invitrogen	Cat#S12375
Collagenase IV	ThermoFisher Scientific	Cat#LS004189
RPMI-1640	RPMI-1640	21870092
Enrofloxacin	Bayer	Baytril 100
Voriconazole	Pfizer	N/A
Tween-20	Sigma	P9416
Protease Inhibitor Cocktail	Roche	Cat#11697498001
DNase I, Grade II	Sigma	Cat#10104159001
isoflurane	Henry Schein Animal Health	Cat#29405
Diphtheria toxin (DT)	List Biological Laboratories	Cat#150
Paraformaldehyde, 32% Solution	ThermoFisher Scientific	Cat#50-980-495
CM-H_2DCFDA	ThermoFisher Scientific	Cat#C6827
10× HBSS	ThermoFisher Scientific	14065056
TRIzol-LS	Invitrogen	10296028
Mouse IFNa2/4 ELISA kit	Invitrogen	BMS6027
Mouse IL-28B/IFN-lambda 3 DuoSet ELISA	Invitrogen	DY1789B-05
Mouse GM-CSF DuoSet ELISA	Invitrogen	DY415-05
Mouse TNF alpha ELISA Ready-SET-Go!™ Kit	Invitrogen	50-173-31

Mouse IL-6 ELISA Ready-SET-Go!™ Kit	Invitrogen	50-172-19
Mouse IL-1 beta ELISA Kit	Invitrogen	BMS6002
Mouse IL-12 p70 ELISA Kit	Invitrogen	BMS6004
High-Capacity RNA-to-cDNA Kit	Appliedbiosystems	4387406
Ribosomal RNA Control Reagents	Appliedbiosystems	4308329
IFNa2 TaqMan Assay Mm00833961_s1	Thermo Fisher	4331182
IFNa1/a5/a6 TaqMan Assay Mm03030145_gH	Thermo Fisher	4331182
IFNL2/3 TaqMan Assay Mm04204155_gH	Thermo Fisher	4331182
Experimental Models: Organisms/Strains		
BDCA2-DTR	The Jackson Laboratory	JAX: 014176
C57BL/6	The Jackson Laboratory	JAX: 000664
C57BL/6.SJL	Taconic	Stock No. 4007
Stat1$^{-/-}$ mice	The Jackson Laboratory	JAX: 012606
GBP$^{chr3-/-}$ mice		Received from Dr. Thirumala-Devi Kanneganti.
Cybb$^{-/-}$ mice	The Jackson Laboratory	JAX: 002365
Software and Algorithms		
Prism 10	Prism 10	N/A
Flow Jo 10.10.0	Flow Jo 10.10.0	N/A

References

Abbas, A., T.P. Vu Manh, M. Valente, N. Collinet, N. Attaf, C. Dong, K. Naciri, R. Chelbi, G. Brelurut, I. Cervera-Marzal, B. Rauwel, J.L. Davignon, G. Bessou, M. Thomas-Chollier, D. Thieffry, A.C. Villani, P. Milpied, M. Dalod, and E. Tomasello. 2020. The activation trajectory of plasmacytoid dendritic cells in vivo during a viral infection. *Nat Immunol* 21:983-997.

Antony, F., C. Pundkar, M. Sandey, A.K. Jaiswal, A. Mishra, A. Kumar, R. Channappanavar, and A. Suryawanshi. 2021. IFN-lambda Regulates Neutrophil Biology to Suppress Inflammation in Herpes Simplex Virus-1-Induced Corneal Immunopathology. *J Immunol* 206:1866-1877.

Antos, D., O.B. Parks, A.M. Duray, N. Abraham, J.J. Michel, S. Kupul, R. Westcott, and J.F. Alcorn. 2024. Cell-intrinsic regulation of phagocyte function by interferon lambda during pulmonary viral, bacterial super-infection. *PLoS Pathog* 20:e1012498.

Ardanuy, J., K. Scanlon, C. Skerry, S.Y. Fuchs, and N.H. Carbonetti. 2020. Age-Dependent Effects of Type I and Type III IFNs in the Pathogenesis of Infection and Disease. *Journal of Immunology* 204:2192-2202.

Assil, S., S. Coleon, C. Dong, E. Decembre, L. Sherry, O. Allatif, B. Webster, and M. Dreux. 2019. Plasmacytoid Dendritic Cells and Infected Cells Form an Interferogenic Synapse Required for Antiviral Responses. *Cell Host Microbe* 25:730-745 e736.

Ballesteros, I., A. Rubio-Ponce, M. Genua, E. Lusito, I. Kwok, G. Fernandez-Calvo, T.E. Khoyratty, E. van Grinsven, S. Gonzalez-Hernandez, J.A. Nicolas-Avila, T. Vicanolo, A. Maccataio, A. Benguria, J.L. Li, J.M. Adrover, A. Aroca-Crevillen, J.A. Quintana, S. Martin-Salamanca, F. Mayo, S. Ascher, G. Barbiera, O. Soehnlein, M. Gunzer, F. Ginhoux, F. Sanchez-Cabo, E. Nistal-Villan, C. Schulz, A. Dopazo, C. Reinhardt, I.A. Udalova, L.G. Ng, R. Ostuni, and A. Hidalgo. 2020. Co-option of Neutrophil Fates by Tissue Environments. *Cell* 183:1282-1297 e1218.

Berry, M.P., C.M. Graham, F.W. McNab, Z. Xu, S.A. Bloch, T. Oni, K.A. Wilkinson, R. Banchereau, J. Skinner, R.J. Wilkinson, C. Quinn, D. Blankenship, R. Dhawan, J.J. Cush, A. Mejias, O. Ramilo, O.M. Kon, V. Pascual, J. Banchereau, D. Chaussabel, and A. O'Garra. 2010. An interferon-inducible neutrophil-driven blood transcriptional signature in human tuberculosis. *Nature* 466:973-977.

Briard, B., R. Karki, R.K.S. Malireddi, A. Bhattacharya, D.E. Place, J. Mavuluri, J.L. Peters, P. Vogel, M. Yamamoto, and T.D. Kanneganti. 2019. Fungal ligands released by innate immune effectors promote inflammasome activation during Aspergillus fumigatus infection. *Nat Microbiol* 4:316-327.

Broggi, A., Y. Tan, F. Granucci, and I. Zanoni. 2017. IFN-lambda suppresses intestinal inflammation by non-translational regulation of neutrophil function. *Nat Immunol* 18:1084-1093.

Brown, G.D., D.W. Denning, N.A. Gow, S.M. Levitz, M.G. Netea, and T.C. White. 2012. Hidden killers: human fungal infections. *Sci Transl Med* 4:165rv113.

Chrysanthopoulou, A., K. Kambas, D. Stakos, I. Mitroulis, A. Mitsios, V. Vidali, I. Angelidou, M. Bochenek, S. Arelaki, A. Arampatzioglou, I.E. Galani, P. Skendros, E.A.Couladouros, S. Konstantinides, E. Andreakos, K. Schafer, and K. Ritis. 2017. Interferon lambda1/IL-29 and inorganic polyphosphate are novel regulators of neutrophil-driven thromboinflammation. *J Pathol* 243:111-122.

727 Desai, J.V., M.A. Zarakas, A.L. Wishart, M. Roschewski, M.A. Aufiero, Á. Donkó, G.
728 Wigerblad, N. Shlezinger, M. Plate, M.R. James, J.K. Lim, G. Uzel, J.R. Bergerson, I.
729 Fuss, R.A. Cramer, L.M. Franco, E.S. Clark, W.N. Khan, D. Yamanaka, G. Chamilos, J.
730 El-Benna, M.J. Kaplan, L.M. Staudt, T.L. Leto, S.M. Holland, W.H. Wilson, T.M. Hohl,
731 and M.S. Lionakis. 2024. BTK drives neutrophil activation for sterilizing antifungal
732 immunity. *J Clin Invest* 134:0021-9738.
733 Dobin, A., C.A. Davis, F. Schlesinger, J. Drenkow, C. Zaleski, S. Jha, P. Batut, M. Chaisson, and
734 T.R. Gingeras. 2013. STAR: ultrafast universal RNA-seq aligner. *Bioinformatics* 29:15-
735 21.
736 Espinosa, V., O. Dutta, C. McElrath, P. Du, Y.J. Chang, B. Cicciarelli, A. Pitler, I. Whitehead,
737 J.J. Obar, J.E. Durbin, S.V. Kotenko, and A. Rivera. 2017. Type III interferon is a critical
738 regulator of innate antifungal immunity. *Sci Immunol* 2:2470-9468.
739 Espinosa, V., A. Jhingran, O. Dutta, S. Kasahara, R. Donnelly, P. Du, J. Rosenfeld, I. Leiner,
740 C.C. Chen, Y. Ron, T.M. Hohl, and A. Rivera. 2014. Inflammatory monocytes
741 orchestrate innate antifungal immunity in the lung. *PLoS Pathog* 10:e1003940.
742 Feys, S., A. Carvalho, C.J. Clancy, J.P. Gangneux, M. Hoenigl, K. Lagrou, B.J.A. Rijnders, L.
743 Seldeslachts, L. Vanderbeke, F.L. van de Veerdonk, P.E. Verweij, and J. Wauters. 2024.
744 Influenza-associated and COVID-19-associated pulmonary aspergillosis in critically ill
745 patients. *Lancet Respir Med* 12:728-742.
746 Fujimura, N., B. Xu, J. Dalman, H. Deng, K. Aoyama, and R.L. Dalman. 2015. CCR2 inhibition
747 sequesters multiple subsets of leukocytes in the bone marrow. *Sci Rep* 5:11664.
748 Gerson, S.L., G.H. Talbot, S. Hurwitz, B.L. Strom, E.J. Lusk, and P.A. Cassileth. 1984.
749 Prolonged granulocytopenia: the major risk factor for invasive pulmonary aspergillosis in
750 patients with acute leukemia. *Ann Intern Med* 100:345-351.
751 Girardin, H., J.P. Latge, T. Srikantha, B. Morrow, and D.R. Soll. 1993. Development of DNA
752 probes for fingerprinting Aspergillus fumigatus. *J Clin Microbiol* 31:1547-1554.
753 Guo, Y., S. Kasahara, A. Jhingran, N.L. Tosini, B. Zhai, M.A. Aufiero, K.A.M. Mills, M.
754 Gjonbalaj, V. Espinosa, A. Rivera, A.D. Luster, and T.M. Hohl. 2020. During
755 Aspergillus Infection, Monocyte-Derived DCs, Neutrophils, and Plasmacytoid DCs
756 Enhance Innate Immune Defense through CXCR3-Dependent Crosstalk. *Cell host &*
757 *microbe* 28:104-116 e104.
758 Hackstein, H., A. Wachtendorf, S. Kranz, J. Lohmeyer, G. Bein, and N. Baal. 2012.
759 Heterogeneity of respiratory dendritic cell subsets and lymphocyte populations in inbred
760 mouse strains. *Respir Res* 13:94.
761 Herbst, S., A. Shah, M. Mazon Moya, V. Marzola, B. Jensen, A. Reed, M.A. Birrell, S. Saijo, S.
762 Mostowy, S. Shaunak, and D. Armstrong-James. 2015. Phagocytosis-dependent
763 activation of a TLR9-BTK-calcineurin-NFAT pathway co-ordinates innate immunity to
764 Aspergillus fumigatus. *EMBO molecular medicine* 7:240-258.
765 Heung, L.J., A. Jhingran, and T.M. Hohl. 2015. Deploying FLAREs to Visualize Functional
766 Outcomes of Host-Pathogen Encounters. *PLoS pathogens* 11:e1004912.
767 Hoenigl, M., D. Seidel, R. Sprute, C. Cunha, M. Oliverio, G.H. Goldman, A.S. Ibrahim, and A.
768 Carvalho. 2022. COVID-19-associated fungal infections. *Nat Microbiol* 7:1127-1140.
769 Hohl, T.M., H.L. Van Epps, A. Rivera, L.A. Morgan, P.L. Chen, M. Feldmesser, and E.G. Pamer.
770 2005. Aspergillus fumigatus triggers inflammatory responses by stage-specific beta-
771 glucan display. *PLoS pathogens* 1:e30.

772 Jhingran, A., S. Kasahara, and T.M. Hohl. 2016. Flow Cytometry of Lung and Bronchoalveolar
773 Lavage Fluid Cells from Mice Challenged with Fluorescent Aspergillus Reporter
774 (FLARE) Conidia. *Bio Protoc* 6:2331-8325.
775 Korotkevich, G., V. Sukhov, and A. Sergushichev. 2019. Fast gene set enrichment analysis.
776 *bioRxiv* 060012.
777 Kumar, A., D. Johnson, A. Bukowski, M.J. Noto, and N.H. Carbonetti. 2024. IFNlambda
778 signaling in neutrophils enhances the pathogenesis of Bordetella pertussis infection. *J*
779 *Leukoc Biol* 0741-5400.
780 Latgé, J.P., and G. Chamilos. 2019. Aspergillus fumigatus and Aspergillosis in 2019. *Clin*
781 *Microbiol Rev* 33:0893-8512.
782 Lazear, H.M., T.J. Nice, and M.S. Diamond. 2015. Interferon-lambda: Immune Functions at
783 Barrier Surfaces and Beyond. *Immunity* 43:15-28.
784 Liao, Y., G.K. Smyth, and W. Shi. 2014. featureCounts: an efficient general purpose program for
785 assigning sequence reads to genomic features. *Bioinformatics* 30:923-930.
786 Lionakis, M.S., R.A. Drummond, and T.M. Hohl. 2023. Immune responses to human fungal
787 pathogens and therapeutic prospects. *Nat Rev Immunol* 23:433-452.
788 Lionakis, M.S., K. Dunleavy, M. Roschewski, B.C. Widemann, J.A. Butman, R. Schmitz, Y.
789 Yang, D.E. Cole, C. Melani, C.S. Higham, J.V. Desai, M. Ceribelli, L. Chen, C.J.
790 Thomas, R.F. Little, J. Gea-Banacloche, S. Bhaumik, M. Stetler-Stevenson, S. Pittaluga,
791 E.S. Jaffe, J. Heiss, N. Lucas, S.M. Steinberg, L.M. Staudt, and W.H. Wilson. 2017.
792 Inhibition of B Cell Receptor Signaling by Ibrutinib in Primary CNS Lymphoma. *Cancer*
793 *Cell* 31:833-843 e835.
794 Lionakis, M.S., and S.M. Levitz. 2018. Host Control of Fungal Infections: Lessons from Basic
795 Studies and Human Cohorts. *Annu Rev Immunol* 36:157-191.
796 Loures, F.V., M. Rohm, C.K. Lee, E. Santos, J.P. Wang, C.A. Specht, V.L. Calich, C.F. Urban,
797 and S.M. Levitz. 2015. Recognition of Aspergillus fumigatus hyphae by human
798 plasmacytoid dendritic cells is mediated by dectin-2 and results in formation of
799 extracellular traps. *PLoS Pathog* 11:e1004643.
800 Love, M.I., W. Huber, and S. Anders. 2014. Moderated estimation of fold change and dispersion
801 for RNA-seq data with DESeq2. *Genome Biol* 15:550.
802 Maldonado, S.D., J. Dai, O. Dutta, H.J. Hurley, S. Singh, L. Gittens-Williams, E. Kalyoussef,
803 K.L. Edelblum, A. Rivera, and P. Fitzgerald-Bocarsly. 2022. Human Plasmacytoid
804 Dendritic Cells Express C-Type Lectin Receptors and Attach and Respond to Aspergillus
805 fumigatus. *J Immunol* 209:675-683.
806 Marciano, B.E., C. Spalding, A. Fitzgerald, D. Mann, T. Brown, S. Osgood, L. Yockey, D.N.
807 Darnell, L. Barnhart, J. Daub, L. Boris, A.P. Rump, V.L. Anderson, C. Haney, D.B.
808 Kuhns, S.D. Rosenzweig, C. Kelly, A. Zelazny, T. Mason, S.S. DeRavin, E. Kang, J.I.
809 Gallin, H.L. Malech, K.N. Olivier, G. Uzel, A.F. Freeman, T. Heller, C.S. Zerbe, and
810 S.M. Holland. 2015. Common severe infections in chronic granulomatous disease. *Clin*
811 *Infect Dis* 60:1176-1183.
812 Mills, K.A.M., M.A. Aufiero, and T.M. Hohl. 2024. Epithelial responses to fungal pathogens.
813 *Curr Opin Microbiol* 80:102508.
814 Montaldo, E., E. Lusito, V. Bianchessi, N. Caronni, S. Scala, L. Basso-Ricci, C. Cantaffa, A.
815 Masserdotti, M. Barilaro, S. Barresi, M. Genua, F.M. Vittoria, G. Barbiera, D. Lazarevic,
816 C. Messina, E. Xue, S. Marktel, C. Tresoldi, R. Milani, P. Ronchi, S. Gattillo, L.
817 Santoleri, R. Di Micco, A. Ditadi, G. Belfiori, F. Aleotti, M.M. Naldini, B. Gentner, E.

Gardiman, N. Tamassia, M.A. Cassatella, A. Hidalgo, I. Kwok, L.G. Ng, S. Crippa, M. Falconi, F. Pettinella, P. Scapini, L. Naldini, F. Ciceri, A. Aiuti, and R. Ostuni. 2022. Cellular and transcriptional dynamics of human neutrophils at steady state and upon stress. *Nat Immunol* 23:1470-1483.

Pollock, J.D., D.A. Williams, M.A. Gifford, L.L. Li, X. Du, J. Fisherman, S.H. Orkin, C.M. Doerschuk, and M.C. Dinauer. 1995. Mouse model of X-linked chronic granulomatous disease, an inherited defect in phagocyte superoxide production. *Nat Genet* 9:202-209.

Preite, N.W., C. Feriotti, D. Souza de Lima, B.B. da Silva, A. Condino-Neto, A. Pontillo, V.L.G. Calich, and F.V. Loures. 2018. The Syk-Coupled C-Type Lectin Receptors Dectin-2 and Dectin-3 Are Involved in Paracoccidioides brasiliensis Recognition by Human Plasmacytoid Dendritic Cells. *Front Immunol* 9:464.

Ramirez-Ortiz, Z.G., C.A. Specht, J.P. Wang, C.K. Lee, D.C. Bartholomeu, R.T. Gazzinelli, and S.M. Levitz. 2008. Toll-like receptor 9-dependent immune activation by unmethylated CpG motifs in Aspergillus fumigatus DNA. *Infection and immunity* 76:2123-2129.

Rocha, B.C., P.E. Marques, F.M.S. Leoratti, C. Junqueira, D.B. Pereira, L. Antonelli, G.B. Menezes, D.T. Golenbock, and R.T. Gazzinelli. 2015. Type I Interferon Transcriptional Signature in Neutrophils and Low-Density Granulocytes Are Associated with Tissue Damage in Malaria. *Cell Rep* 13:2829-2841.

Seeds, R.E., S. Gordon, and J.L. Miller. 2009. Characterisation of myeloid receptor expression and interferon alpha/beta production in murine plasmacytoid dendritic cells by flow cytomtery. *J Immunol Methods* 350:106-117.

Shlezinger, N., H. Irmer, S. Dhingra, S.R. Beattie, R.A. Cramer, G.H. Braus, A. Sharon, and T.M. Hohl. 2017. Sterilizing immunity in the lung relies on targeting fungal apoptosis-like programmed cell death. *Science* 357:1037-1041.

Sozzani, S., W. Vermi, A. Del Prete, and F. Facchetti. 2010. Trafficking properties of plasmacytoid dendritic cells in health and disease. *Trends Immunol* 31:270-277.

Subramanian, A., P. Tamayo, V.K. Mootha, S. Mukherjee, B.L. Ebert, M.A. Gillette, A. Paulovich, S.L. Pomeroy, T.R. Golub, E.S. Lander, and J.P. Mesirov. 2005. Gene set enrichment analysis: a knowledge-based approach for interpreting genome-wide expression profiles. *Proc Natl Acad Sci U S A* 102:15545-15550.

Swiecki, M., S. Gilfillan, W. Vermi, Y. Wang, and M. Colonna. 2010. Plasmacytoid dendritic cell ablation impacts early interferon responses and antiviral NK and CD8(+) T cell accrual. *Immunity* 33:955-966.

Swiecki, M., H.L. Miller, R. Sesti-Costa, M. Cella, S. Gilfillan, and M. Colonna. 2017. Microbiota induces tonic CCL2 systemic levels that control pDC trafficking in steady state. *Mucosal Immunol* 10:936-945.

Taylor, P.R., G.D. Brown, D.M. Reid, J.A. Willment, L. Martinez-Pomares, S. Gordon, and S.Y. Wong. 2002. The beta-glucan receptor, dectin-1, is predominantly expressed on the surface of cells of the monocyte/macrophage and neutrophil lineages. *J Immunol* 169:3876-3882.

Thompson, G.R., 3rd, and J.H. Young. 2021. Aspergillus Infections. *N Engl J Med* 385:1496-1509.

Tischler, B.Y., and T.M. Hohl. 2019. Menacing Mold: Recent Advances in Aspergillus Pathogenesis and Host Defense. *J Mol Biol* 431:4229-4246.

Varughese, T., Y. Taur, N. Cohen, M.L. Palomba, S.K. Seo, T.M. Hohl, and G. Redelman-Sidi. 2018. Serious Infections in Patients Receiving Ibrutinib for Treatment of Lymphoid Cancer. *Clin Infect Dis* 67:687-692.

Webster, B., S.W. Werneke, B. Zafirova, S. This, S. Coleon, E. Decembre, H. Paidassi, I. Bouvier, P.E. Joubert, D. Duffy, T. Walzer, M.L. Albert, and M. Dreux. 2018. Plasmacytoid dendritic cells control dengue and Chikungunya virus infections via IRF7-regulated interferon responses. *Elife* 7:2050-2084X

Xie, X., Q. Shi, P. Wu, X. Zhang, H. Kambara, J. Su, H. Yu, S.Y. Park, R. Guo, Q. Ren, S. Zhang, Y. Xu, L.E. Silberstein, T. Cheng, F. Ma, C. Li, and H.R. Luo. 2020. Single-cell transcriptome profiling reveals neutrophil heterogeneity in homeostasis and infection. *Nat Immunol* 21:1119-1133.

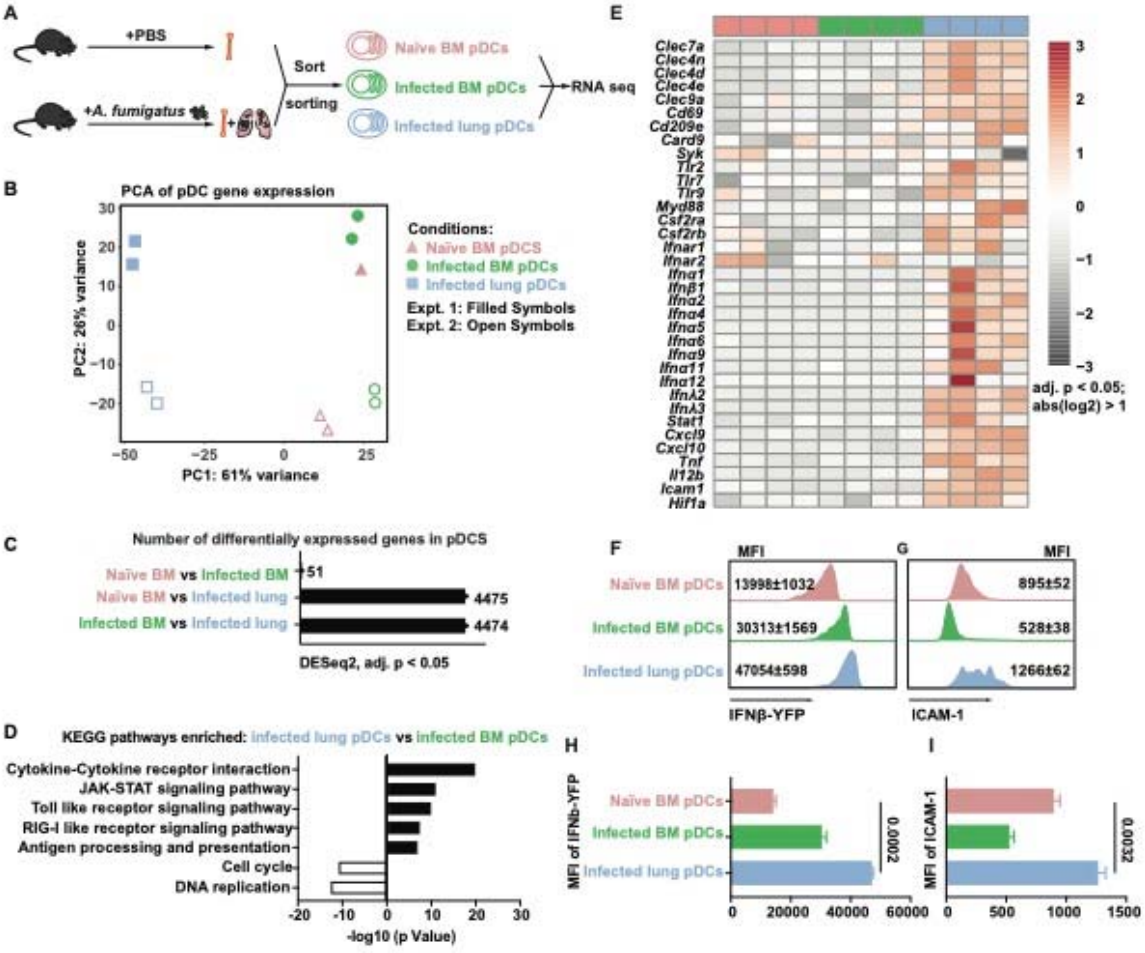

Figure 1. pDC transcriptome following *A. fumigatus* infection.

(A) Experimental scheme for bulk RNA-seq of BM pDCs sorted from naïve mice (red symbols) and BM (green symbols) and lung (blue symbols) pDCs sorted from *A. fumigatus*-infected mice. (B) Principal component analysis of gene expression in sorted BM pDCs from naïve (triangles) and infected mice (dots) and of sorted lung pDCs from infected mice (squares). Each symbol represents a biological replicate. pDCs from 10 mice were pooled for each replicate, and 2 replicates were included in each of 2 experiments, denoted as Expt1 (filled symbol) and Expt 2 (open symbols). (C) Number of differentially expressed genes for three comparisons of 2 pDC subsets. (D) Differentially enriched KEGG pathways ($q < 0.05$) in pDCs isolated from infected

885 lungs vs infected BM. Black bars indicate pathways enriched in lung pDCs from infected mice,
886 white bars indicate pathways enriched in BM pDCs from infected mice. (E) Heatmap for 35
887 selected genes with a >2 -fold difference in expression and a false discovery rate (FDR) $p < 0.05$.
888 Each lane represents 1 replicate from 2 expts. (F - I) Representative flow cytometry plots (F and
889 G) and quantified mean fluorescence intensity MFI (H and I) of IFNβ-YFP and ICAM-1
890 expression in pDCs isolated from (top) naïve BM, (middle), the BM of *A. fumigatus*-infected
891 mice or (bottom) the lungs of *A. fumigatus*-infected mice. (A-I) Infection dose: 3×10^7 CEA10
892 conidia via intratracheal route, analysis 72 hpi. (B - E) Data were pooled from 2 independent
893 experiments. (H and I) Statistical analysis: Kruskal-Wallis test. See also Figure S1.

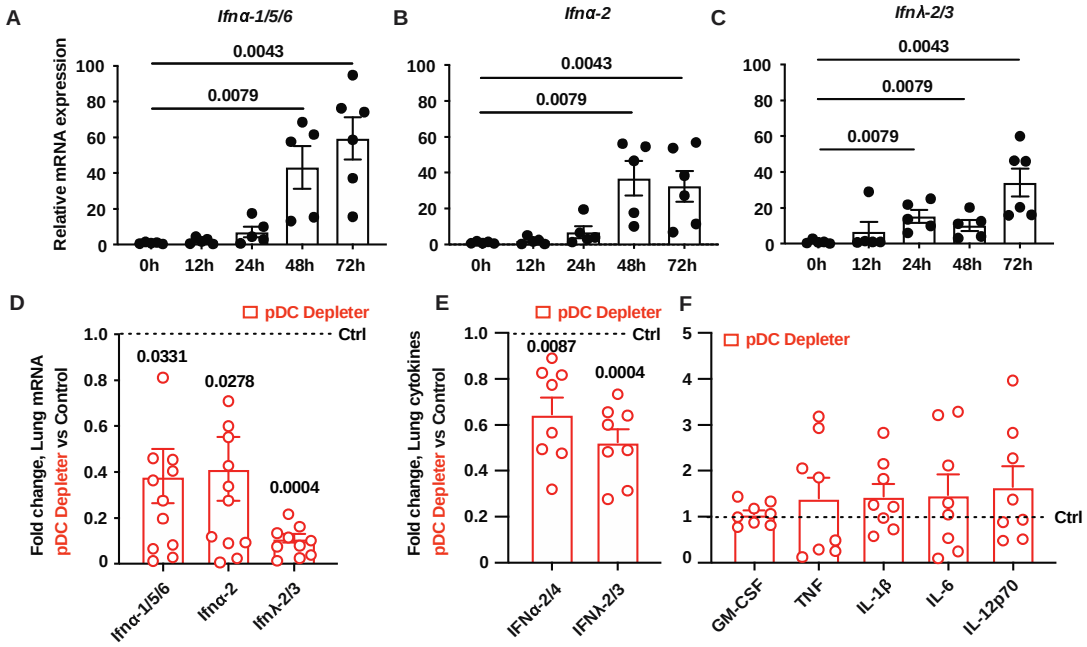

Figure 2. Cytokine profiles in pDC-depleted mice during *A. fumigatus* infection

(A - C) *Ifn* gene expression, measured by qRT-PCR using TaqMan probes, in the lung of C57BL6/J mice at indicated times, n = 5-6 per group. (D) Lung *Ifn* gene expression and (E and F) lung cytokine levels measured by ELISA in DT-treated pDC depleter mice (BDCA2-DTR$^{Tg/+}$; red symbols) and DT-treated non-Tg littermate controls (black dashed line), n = 8 per group. (A - E) Infection dose: 3×10^7 CEA10 conidia via intratracheal route, analysis 72 hpi. Data were pooled from 2 independent experiments and presented as mean ± SEM. Dots represent individual mice. Statistical analysis: Kruskal-Wallis test

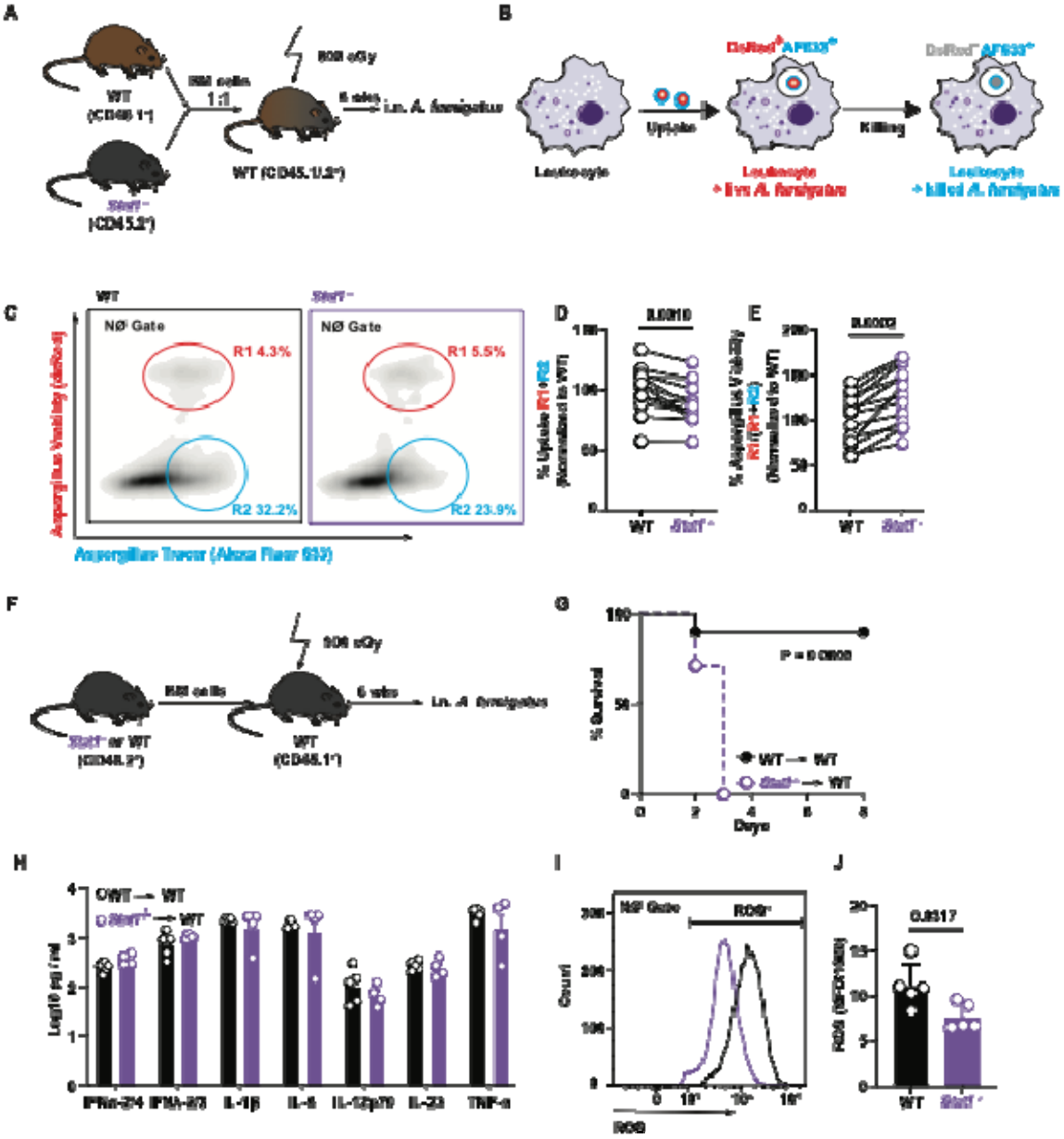

Figure 3. STAT1 signaling regulates neutrophil-intrinsic *Aspergillus* killing.

(A) Scheme to generate *Stat1*$^{-/-}$ and *Stat*$^{+/+}$ mixed bone chimeric mice and (B) illustration of the two-component fluorescent *Aspergillus* reporter (FLARE) system used to measure conidial uptake and killing by *Stat1*$^{-/-}$ and *Stat*$^{+/+}$ lung leukocytes in mixed bone marrow chimeric mice. (C) Representative plot that display DsRed and AF633 fluorescence intensity of lung neutrophils.

910 The R1 gate denotes neutrophils that contain live conidia, the R2 gate denotes neutrophils that
911 contain killed conidia. (D and E) The plots show (D) normalized lung neutrophil conidial uptake
912 (R1 + R2) ± SEM and (E) conidial viability (R1/ (R1 + R2) ± SEM in indicated lung neutrophils
913 isolated from *Stat1*$^{-/-}$ (purple symbols) and *Stat1*$^{+/+}$(black symbols) mixed BM chimeric mice
914 (n=8 per group). (F) Scheme to generate *Stat1*$^{-/-}$ and WT (*Stat*$^{+/+}$) chimeric mice. (G) Kaplan
915 Meier survival of *Stat1*$^{-/-}$ and *Stat*$^{+/+}$ chimeric mice (n = 7-8 per group) infected with 3-6 × 10^7
916 CEA10 conidia. (H) Lung cytokine levels in *Stat1*$^{-/-}$ → WT (purple symbols) and *Stat1*$^{+/+}$→ WT
917 (black symbols) single chimeric mice. (I) Representative plot and (J) mean ± SEM neutrophil
918 ROS production in cells isolated from *Stat1*$^{-/-}$ → WT (purple symbols) and *Stat1*$^{+/+}$→ WT (black
919 symbols) single chimeric mice (n=5 per group). (C - E) Infection dose: 3 × 10^7 Af293 FLARE
920 conidia via intratracheal route, analysis 72 hpi. (F - I) Infection dose: 3 × 10^7 CEA10 conidia via
921 intratracheal route, analysis 72 hpi. (D and E) Data were pooled from 2 independent experiments.
922 Dots represent individual mice. Statistical analysis: paired t test. (H - J) Data are representative
923 of 2 experiments. Dots represent individual mice. Statistical analysis: Mann-Whitney test. See
924 also Figure S2.

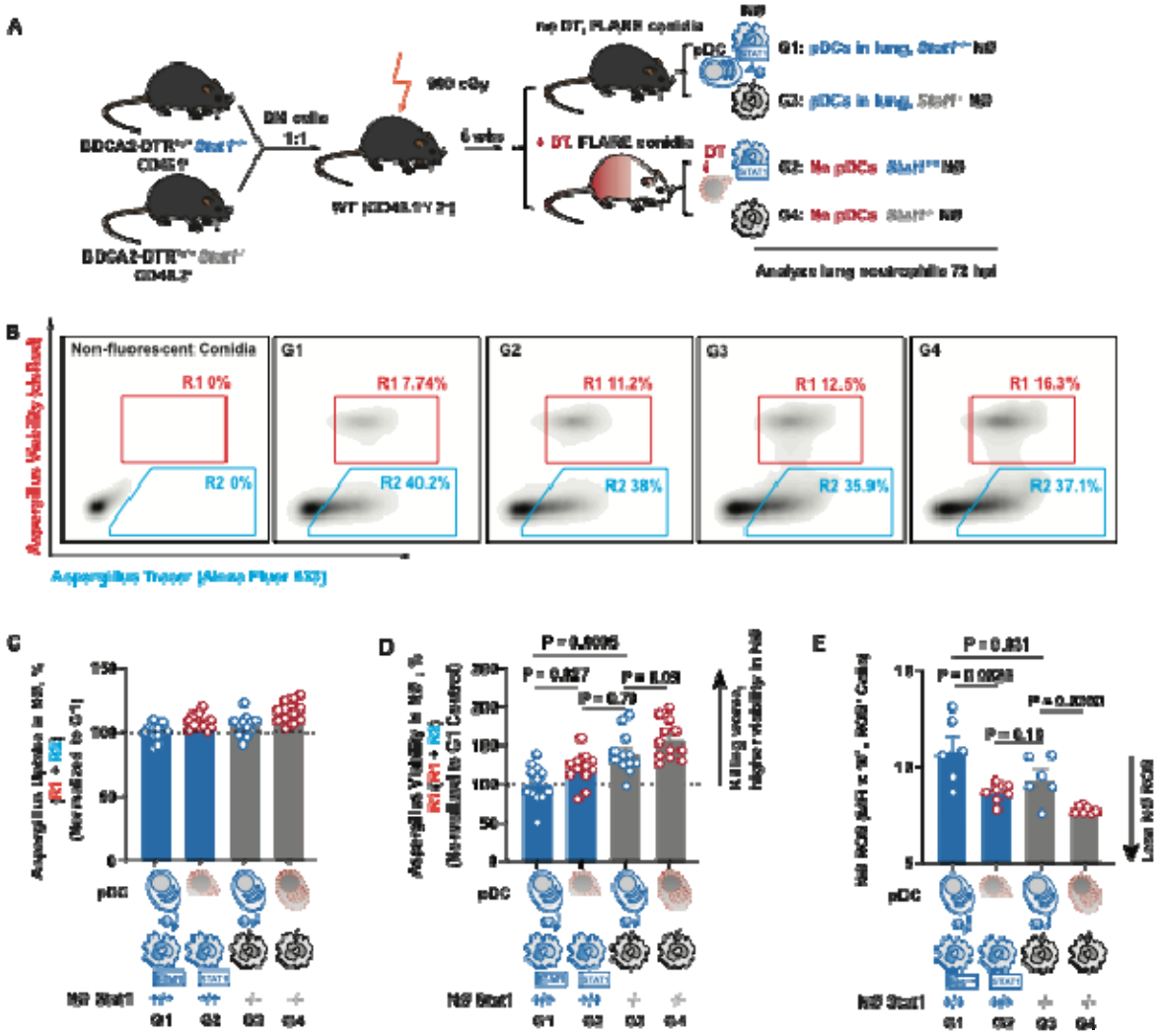

925

926 **Figure 4. pDCs regulate neutrophil STAT1-dependent antifungal activity.**

927 (A) Scheme to generate and to deplete pDCs or not in CD45.1^{+} BDCA2- DTR$^{Tg/+}$ *Stat1*$^{+/+}$ and

928 CD45.2^{+} BDCA2- DTR$^{Tg/+}$ *Stat1*$^{-/-}$ mixed bone marrow chimeric mice, resulting in 4

929 experimental groups (G1-G4). (B-D) (B) Representative plots that display DsRed and Af633

930 fluorescence intensity in lung neutrophils from 4 experimental groups: G1: pDC^{+} *Stat1*$^{+/+}$

931 (*Stat1*$^{+/+}$ neutrophils from pDC-sufficient mice), G2: pDC^{-} *Stat1*$^{+/+}$ (*Stat1*$^{+/+}$ neutrophils from

932 pDC-depleted mice), G3: pDC^{+} *Stat1*$^{-/-}$ (*Stat1*$^{-/-}$ neutrophils from pDC-sufficient mice), G4: pDC^{-}

933 *Stat1*$^{-/-}$ (*Stat1*$^{-/-}$ neutrophils from pDC-depleted mice). The R1 gate indicates the frequency of
934 neutrophils that contain live conidia, the gate R2 indicates the frequency of neutrophils that
935 contain killed conidia. (C and D) The plots show mean neutrophil (C) conidial uptake (R1 + R2)
936 ± SEM and (D) conidial viability (R1/ (R1 + R2) ± SEM in indicated lung neutrophils isolated
937 from the 4 groups, n = 12 per group, data pooled from 2 experiments. (E) Mean ± SEM ROS
938 production in indicated lung neutrophils, n = 6 per group. (B - D) Infection dose: 3×10^7 Af293
939 FLARE conidia via intratracheal route, analysis 72 hpi. (C and D) Data were pooled from 2
940 independent experiments and presented as mean ± SEM, (E) Data are representative of 2
941 experiments. Dots represent individual mice. Statistical analysis: Kruskal-Wallis test. See also
942 Figure S3.
943

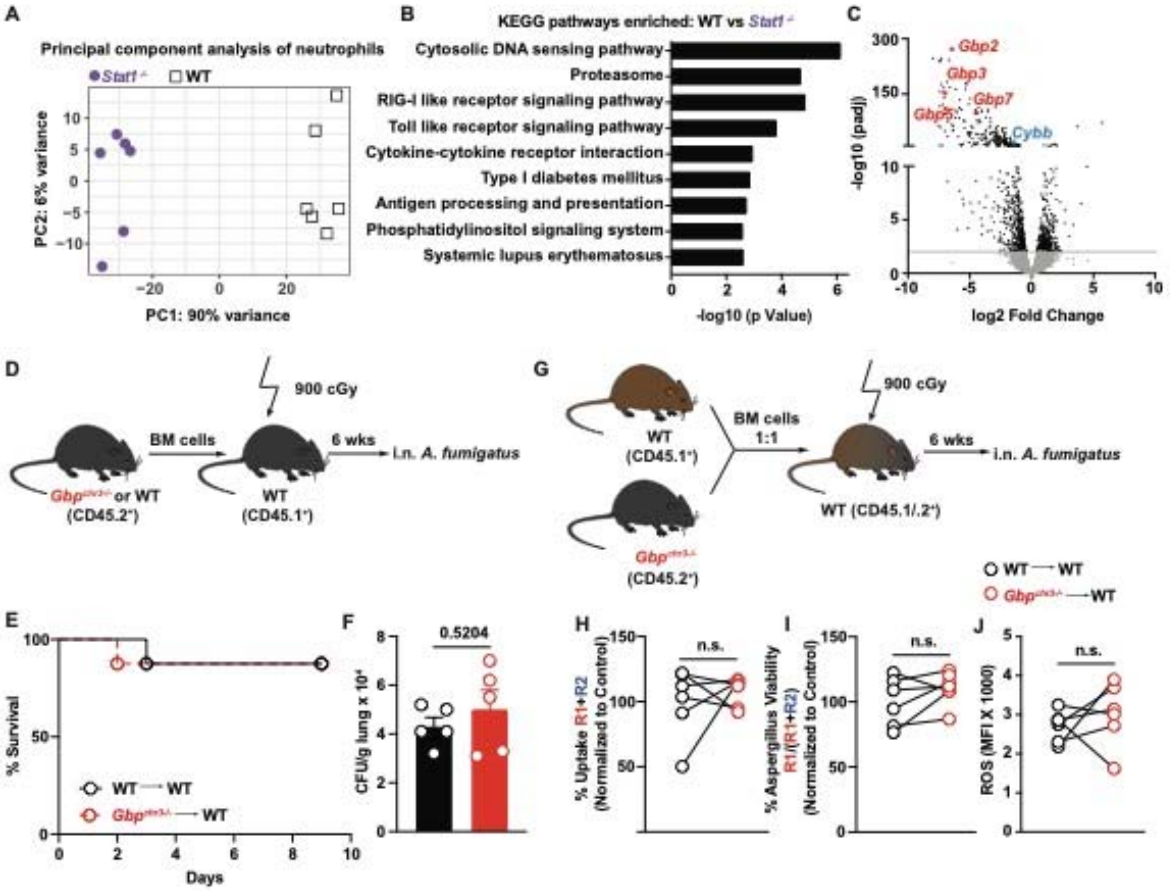

Figure 5. STAT1-dependent guanylate-binding proteins are dispensable for the neutrophil antifungal response.

(A) Principal component analysis of global gene expression, (B) differentially enriched KEGG pathways, and (C) Volcano plot of differentially expressed genes in *Stat1*$^{-/-}$ (purple symbols) and *Stat1*$^{+/+}$(black symbols) neutrophil sorted from mixed bone marrow chimeric mice (n = 6) at 72 hpi with 3 × 10^7 CEA10 conidia. Selected downregulated genes in *Stat1*$^{-/-}$ neutrophils are highlight in the Volcano plot. (D) Experimental scheme to generate *GBP*$^{chr3-/-}$ and *GBP*$^{chr3+/+}$ single chimeric mice. (E) Kaplan Meier survival (n = 7-8 per group), and (F) mean ± SEM lung CFU (n = 5 per group) in *GBP*$^{chr3-/-}$ (red symbols) and *GBP*$^{chr3+/+}$ (black symbols) single chimeric mice infected with 3-6 × 10^7 CEA10 conidia. (G) Experimental scheme to generate

955 *GBP*$^{chr3-/-}$ and *GBP*$^{chr3+/+}$ mixed chimeric mice. (H and I) The plots show normalized neutrophil
956 (H) conidial uptake (R1 + R2) ± SEM and (I) conidial viability (R1/ (R1 + R2) ± SEM in lung
957 neutrophils isolated from *GBP*$^{chr3-/-}$ (red symbols) and *GBP*$^{chr3+/+}$ (black symbols) mixed bone
958 marrow chimeric mice (n = 6 per group). (J) Mean ± SEM neutrophil ROS production in
959 neutrophils isolated from *GBP*$^{chr3-/-}$ (red symbols) and *GBP*$^{chr3+/+}$ (black symbols) mixed bone
960 marrow chimeric mice (n=6 per group). (H - J) Infection dose: 3×10^7 Af293 FLARE conidia
961 via intratracheal route, analysis 72 hpi. (F, H - J) Data are representative of 2 experiments and
962 presented as mean ± SEM. Dots represent individual mice. Statistical analysis: Mann-Whitney
963 test.
964

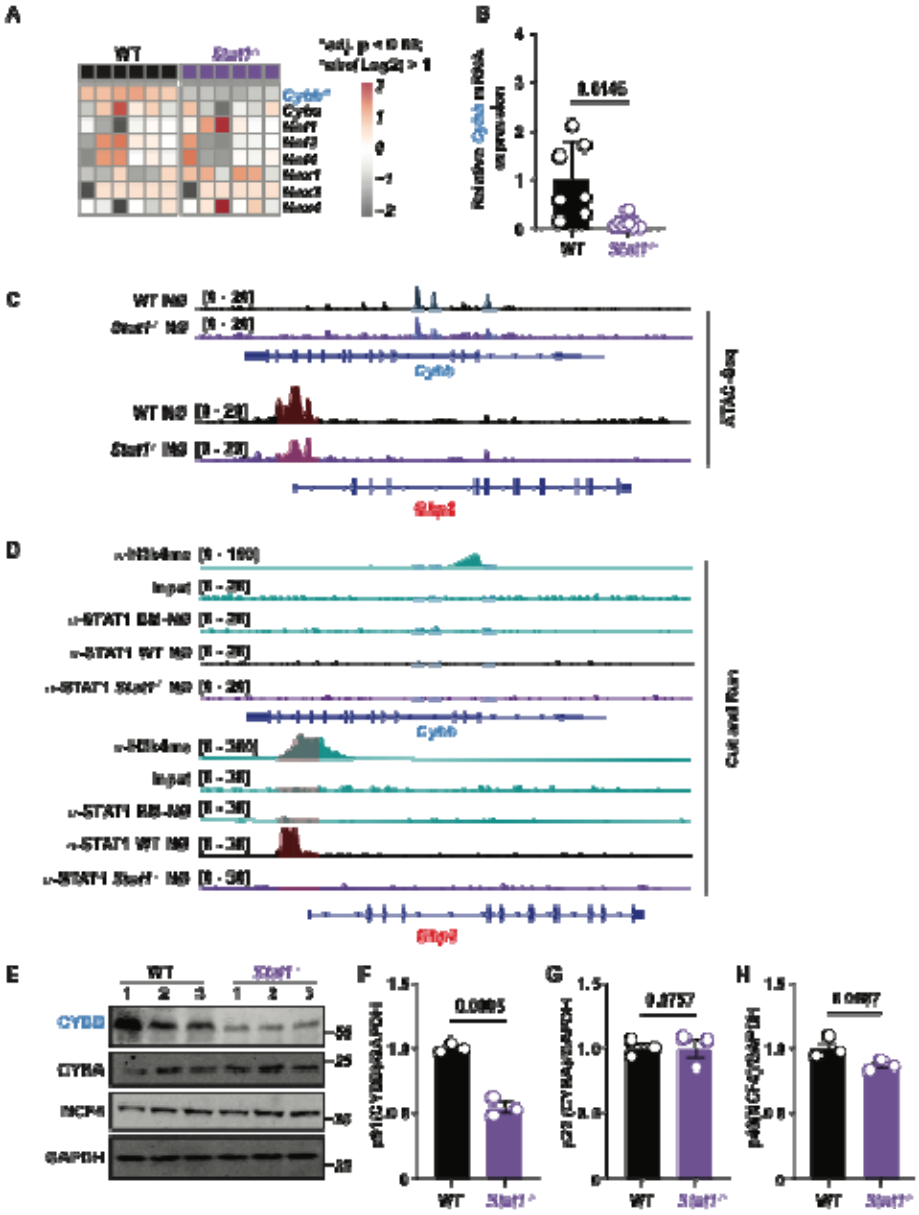

Figure 6. STAT1-dependent control of *Cybb* expression and CYBB protein levels in neutrophils.

(A) Heatmap of *Cybb*, *Cyba*, *Ncf1*, *Ncf3*, *Ncf4*, *Nox1*, *Nox3*, and *Nox4* expression in neutrophils sorted from *Stat1*$^{-/-}$ (purple symbols) and *Stat1*$^{+/+}$ (black symbols) mixed bone marrow chimeric mice (n = 6). Genes with a STAR* are DEG. Each lane is an independent biological replicate. (B) qRT-PCR of *Cybb* mRNA expression in neutrophils sorted from *Stat1*$^{-/-}$ (purple symbols) and

Stat1$^{+/+}$ (black symbols) mice. (C) ATAC-seq analysis of neutrophils were sorted from *Stat1*$^{-/-}$ (purple peaks) and *Stat*$^{+/+}$ (black peaks) mice. Gene tracks show chromatin accessibility at the *Cybb* and *Gbp2* locus. (D) Bone marrow and lung neutrophils were sorted from *Stat1*$^{-/-}$ (purple peaks) and *Stat1*$^{+/+}$ (black peaks) mice and processed for CUT&RUN. Gene tracks show STAT1 signal as normalized fragment pileup (y-axis) plotted by genome position (x-axis). The shaded box highlights a putative STAT1 binding site at the Gbp2 promoter region. Gene tracks show H3K4me3 ChIP-seq signal as normalized fragment pileup (top rows; green). (E - H) Western blot and quantitation of (F) CYBB, (G) CYBA, (H) NCF4 vs GAPDH protein levels in lung neutrophils sorted from *Stat1*$^{-/-}$ (purple symbols) and *Stat1*$^{+/+}$ (black symbols) mice, neutrophils from 4-5 mice were pooled to obtain sufficient protein for Western blot analysis in each biological replicate. (A - H) Infection dose: 3×10^7 CEA10 conidia via intratracheal route, analysis 72 h pi. (C) Data were calculated by Kruskal-Wallis nonparametric test for multiple comparisons for each group compared with control group. (G – I) Data are representative of 2 experiments. Dots represent individual mice. Statistical analysis: Mann-Whitney test. See also Figure S4.

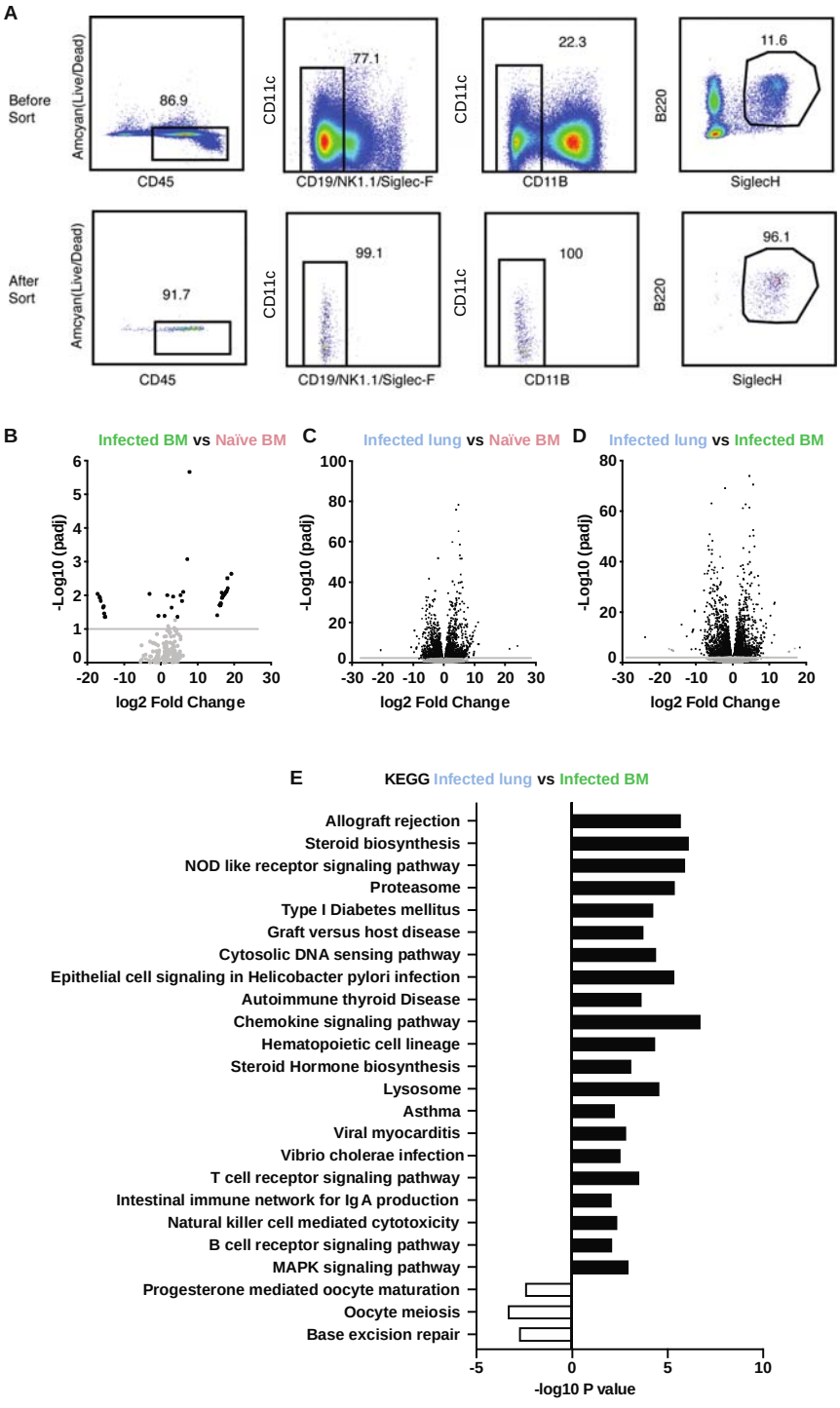

Figure S1. Related to Fig. 1. pDC transcriptome analysis following *A. fumigatus* infction.

(A) The plots indicate the FACS sorting strategy for BM and lung pDCs (top row) and the typical (>95%) pDC purity after FACS sorting (bottom row). (B) Volcano plot of the

992 differentially expressed genes in pDCs sorted from the bone marrow of infected vs. naïve mice.
993 (C) Volcano plot of the differentially expressed genes in pDCs sorted from infected lungs vs
994 naïve bone marrow. (D) Volcano plot of the differentially expressed genes in pDCs sorted from
995 infected lungs vs infected bone marrow. (E) The plot shows differentially exriched KEGG
996 pathways ($q < 0.05$) observed in pDCs isolated from infected lungs vs infected BM. Black
997 bars indicate pathways enriched in lung pDCs from infected mice, white bars indicate pathways
998 enriched in BM pDCs from infected mice.

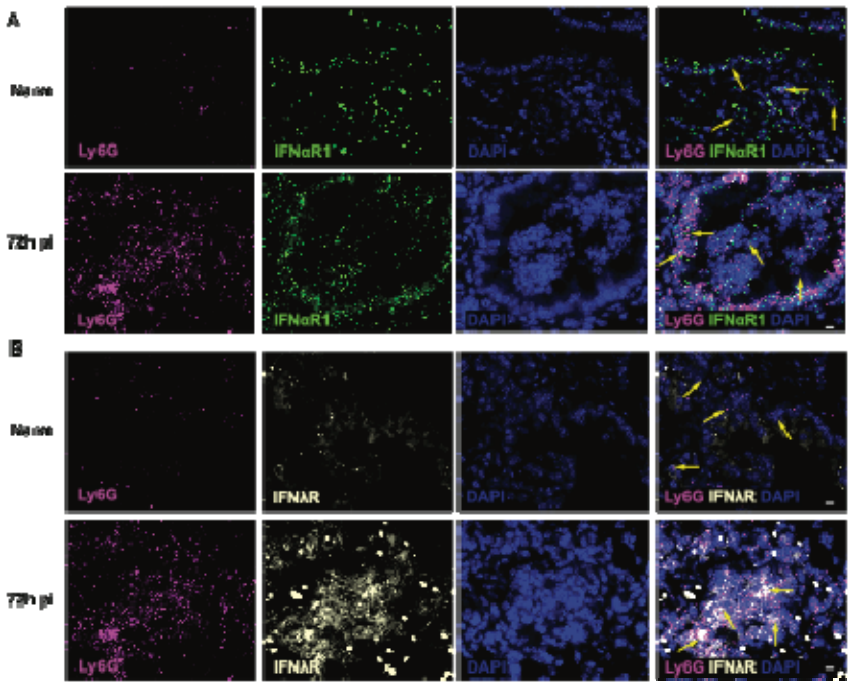

Figure S2. Related to Fig. 3. Type I and III IFN receptor expression on Ly6G$^+$ lung neutrophils.

(A) Lung sections from naïve and *A. fumigatus*-infected mice were analyzed by RNAscope using probes to Ly6G (first column) and IFNαR1 (second column), and DAPI (third column), and merged images are shown in fourth column, and yellow arrows indicate examples of co-localization of the Ly6G and IFNαR1 probes within the same nuclei. (B) Lung sections from naïve and *A. fumigatus*-infected mice were analyzed by RNAscope using probes to Ly6G (first column) and IFNλR1 (second column), and DAPI (third column), and merged images are shown in fourth column, and yellow arrows indicate examples of co-localization of the Ly6G and IFNλR1 probes within the same nuclei. (A and B) Infection dose: 3×10^7 CEA10 conidia via intratracheal route, analysis at 72 hpi. Scale bar = 20 μm.

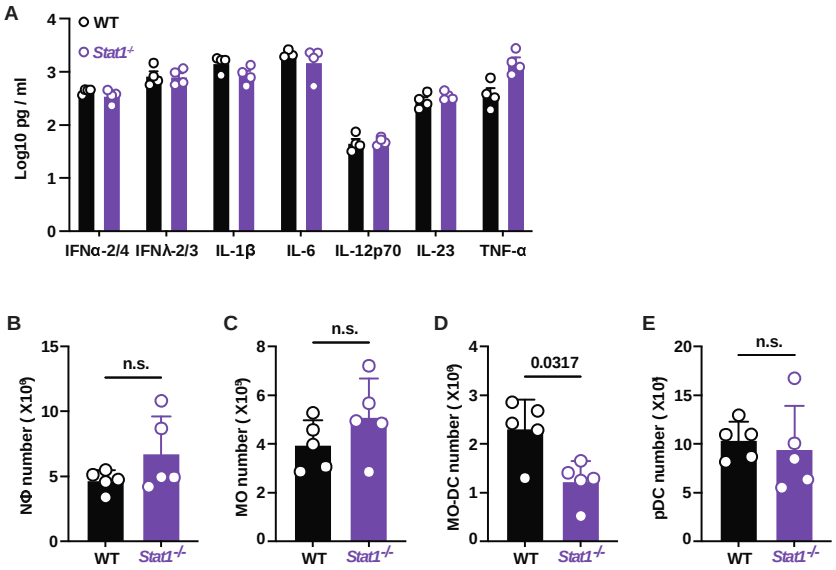

Figure S3. Related to Fig. 4. STAT1 modulates the neutrophil antifungal response.

(A) Lung cytokine levels measured by ELISA of *Stat1*$^{-/-}$ (purple symbols) and *Statt1*$^{+/+}$(black symbols) mice. (B - E) Lung (B) neutrophil, (C) monocyte, (D) Mo-DC and (E) pDC numbers in *Stat1*$^{-/-}$ (purple symbols) and *Stat1*$^{+/+}$ (black symbols). (A - E) Infection dose: 3×10^7 CEA10 conidia via intratracheal route, analysis 72 hpi. Data are representative of 2 experiments. Dots represent individual mice. Statistical analysis: Mann-Whitney test.

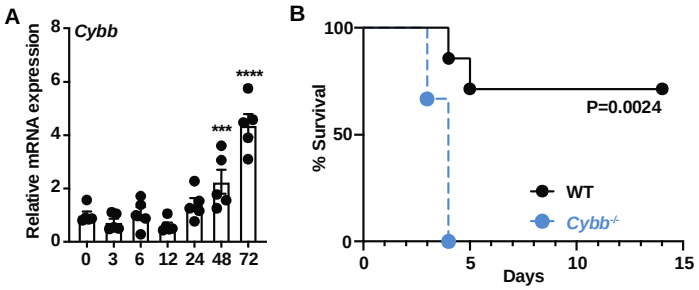

Figure S4. Related to Fig. 6. *Cybb*$^{-/-}$ mice are susceptible to *A. fumigatus* infection.

(A) *Cybb* gene expression in neutrophils isolated from *Stat1*$^{-/-}$ (purple symbols) and *Stat1*$^{+/+}$ (black symbols) mice. Gene expression as determined by qRT-PCR (n = 3 - 5 per group) (B) Kaplan Meier survival (n = 7 - 8 per group) of *Cybb*$^{-/-}$ (blue symbols) and WT control (black symbols) mice infected with 3 - 6 × 10^7 CEA10 conidia. (C) Genome browser tracks of ATAC-seq data at the *Cybb* locus in lung neutrophils isolated from *Stat1*$^{-/-}$ (purple symbols) and *Stat*$^{+/+}$(black symbols) mice. (D) Statistics of peaks at indicated *Cybb* loci in lung neutrophils isolated from *Stat1*$^{-/-}$ (purple symbols) and *Stat*$^{+/+}$ (black dash line) mice. (A - D) Infection dose: 3 × 10^7 CEA10 conidia via intratracheal route, analysis 72 hpi. *P < 0.05; **P < 0.01; ***P < 0.001. Data presented as mean ± SEM. Dots represent individual mice. Statistical analysis: Kruskal-Wallis test for multiple comparisons.

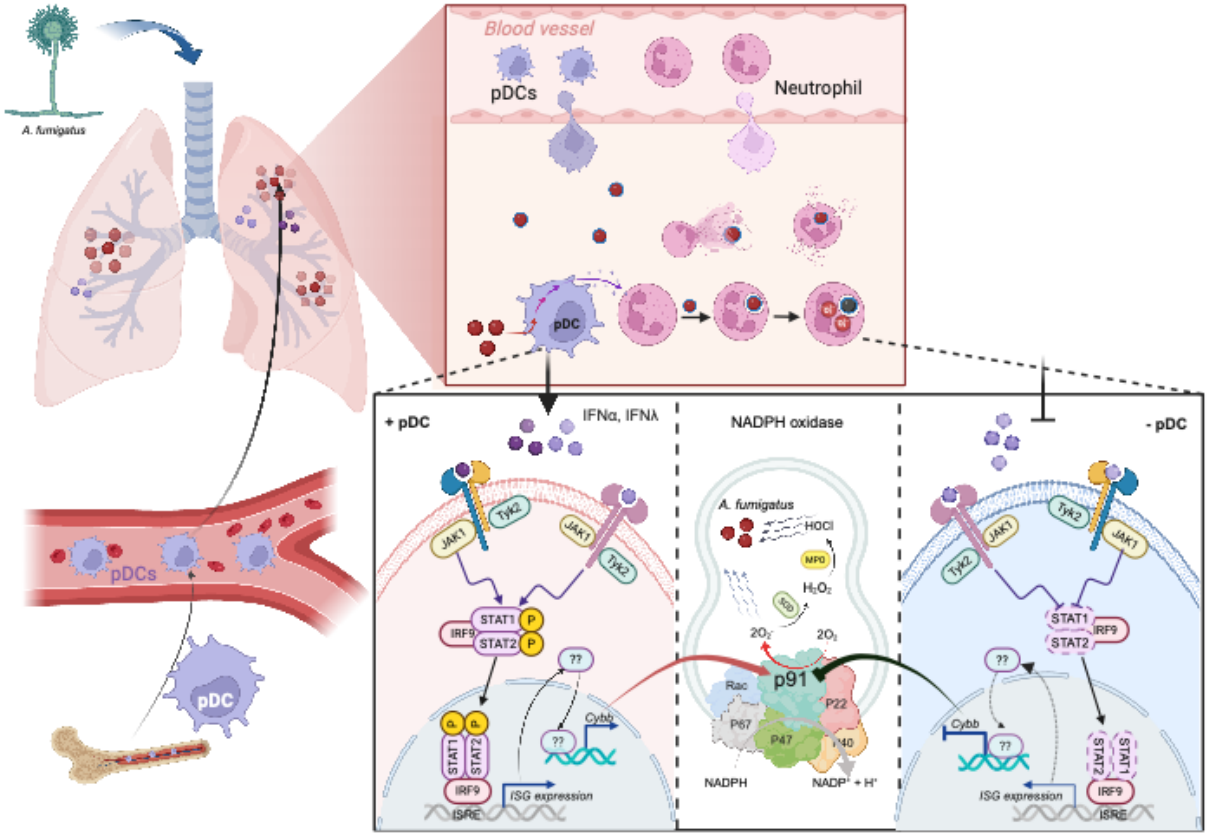

Graphic abstract

- pDC activation in the infected lung coincides with type I and type III interferon production.
- pDCs represent a major, but not exclusive source of type I and type III IFN in the *Aspergillus*-infected lung.
- These pDC-derived products act on type I and type III IFN receptor$^+$ lung neutrophils via STAT1 signal transduction.
- STAT1-dependent neutrophil fungal killing and ROS production is attenuated in the absence of pDCs.
- STAT1 expression regulates *Cybb* transcription and CYBB protein levels in neutrophils, but does not regulate the transcription or translation of other subunits of neutrophil NADPH oxidase.